Engineering Fracture Mechanics 277 (2023) 108949

Contents lists available at ScienceDirect

Engineering Fracture Mechanics

journal homepage: www.elsevier.com/locate/engfracmech

# A comprehensive characterization of fracture in unit cell open foams generated from Triply Periodic Minimal Surfaces

Deison Préve [a,*], Pietro Lenarda [a,*], Ian Maskery [b], Marco Paggi [a]

[a] IMT School for Advanced Studies Lucca, Piazza San Francesco 19, 55100 Lucca, Italy
[b] Centre for Additive Manufacturing, Faculty of Engineering, University of Nottingham, Nottingham NG7 2RD, UK

ARTICLE INFO

*Keywords:*
Phase-field modelling
Brittle fracture
Triply Periodic Minimal Surfaces
Finite Element Method FEM
Fracture mechanics
Open foams

ABSTRACT

The main scope of the proposed study is to assess the occurrence of fracture in Triply Periodic Minimal Surfaces (TPMS) foams subjected to compressive loading. TPMS, developed by the mathematics community, may be exploited as a backbone for developing a new class of foams with open porosity for a wide range of engineering and biomedical applications. Therefore, a comprehensive analysis of their fracture response is fundamental and is herein attempted. To this aim, a 3D phase field model is herein proposed and applied to TPMS foam structures under compression, with the goal to predict critical points for crack nucleation, potential crack paths, and the stiffness and maximum force of the unit cell, which can be related to the apparent Young's modulus and apparent strength of a macro-scale composite made of such TPMS unit cells. A careful mesh sensitivity analysis was conducted on the specimens, to provide guidelines on how to identify the optimal finite element discretization consistent with the internal length scale parameter of the phase field approach to fracture. The major predicted mechanical properties for five different TPMS open foams, and for different levels of porosity, are summarized in Ashby plots. The predicted trends are in agreement with previous results on TPMS taken from the literature and show that TPMS can outperform standard Aluminium open foams.

## 1. Introduction

A minimal surface can be interpreted as a surface that is locally area minimizing when a boundary curve is given, specifically they may also be defined as surfaces with zero mean curvature [1,2]. Started by Plateau's experiments over surface tension with soap films in the mid of the 19th Century, which had demonstrated the existence of stable surfaces with least area bounded by a closed curve. Lately, resolving Plateau's problem regards to the minimization of the energetic cost of the surface, since the total interfacial energy depends on the amount of interface, and hence, on the principal curvatures [3]. Intuitively, a legitimate question rises, beside soap films, whether such behaviour is reproduced by nature. Indeed, minimal surfaces are frequently seen in natural objects, for instance, in beetle shells, weevils, butterfly wing scales [4], crustacean skeletons [5–9], trabecular bone [10,11], whose interface presents mean curvature near to zero everywhere.

In this context, Triply Periodic Minimal Surfaces (TPMS) are minimal surfaces which have periodicity throughout the three space dimensions. TPMS struts are flourishing as objects of great interest to physicists, biologists, and mathematicians [12,13]. From the standing point of mechanics, it has proved TPMS are not only geometrically extremal but extremal for heat transport,

* Corresponding authors.
*E-mail addresses:* deison.preve@imtlucca.it (D. Préve), pietro.lenarda@imtlucca.it (P. Lenarda), ian.maskery@nottingham.ac.uk (I. Maskery), marco.paggi@imtlucca.it (M. Paggi).

https://doi.org/10.1016/j.engfracmech.2022.108949
Received 15 July 2022; Received in revised form 21 September 2022; Accepted 16 November 2022
Available online 25 November 2022

electric conduction, and permeability [14–18]. They also showed enhanced mechanical properties when compared to other cellular structures, and thus are promising candidates for various technological applications [19,20]. Thanks to developed automated assembly and additive manufacturing (AM) techniques [21–24], progress have been made in manufacturing TPMS cellular materials for engineering applications, permeability for bone tissue engineering and orthopaedic applications [25–31], showing significant potential benefits.

Experimental studies in quasi-static compression have been proposed [19,28,32–35] physical and mechanical responses of TPMS lattices, as aforementioned. The effect of the volume fraction (also defined as the complement to unity of porosity) has also been scrutinized [36–39]. Numerical results by [40] have shown that a volume fraction of 30% is desirable for cell in-growth in bone tissue engineering. The energy absorption ability of some graded and uniform TPMS specimens made via AM were discussed in [22,41], whereby also micro-cracks were registered during compression tests. Mechanical properties were derived through AM fabricated TPMS lattices having Titanium alloy Ti–6Al–4V [26,27,42], and Aluminium alloy Al–Si10–Mg [43,44], as main materials. In the latter, it was stated that choosing a small unit cell size can avoid low-strain structural failure caused by localized fracture and crack propagation. In addition, thereby it has been stated that due to the complex geometry, the crack initiation site is difficult to be spotted, as well as the crack paths were complicated to be determined. At this point, it is worthy noting that inherent problems of different AM techniques and different microstructure properties of the material might lead to different crack patterns, where inevitable micro defects from the fabrication process might serve as nucleation sites [45]. For instance, in [46], it was noted that excess of Ti–6Al–4V alloy powders adhered to the surface of the sample led to a thicker sheet, affecting the geometry accuracy and roughness of the fabricated specimens. In [28], microscopic images showed crack formation sites at manufacturing imperfections and at small pores in the bulk. Besides, due to the TPMS continuous rate of curvature, TPMS cells do not have notches (sharp zones), which can act as stress concentrators, minimizing crack nucleation sites from staircase effect inherent to AM techniques [47]. By so, TPMS tend to present improved fatigue resistance in comparison to other conventional lattice structures (truss-based) with the same volume fraction.

So far, the majority of simulation work for structural integrity analysis of TPMS has been confined to the identification of elastic instabilities and plasticity [32,40,48,49]. Therefore, the present work aims at exploiting the phase field approach to fracture to numerically tackle the above open issues, assessing/estimating crack sites, nucleation, propagation and branching under uniaxial compressive loads in TPMS open foams.

In the pioneering formulation in [50], the entire quasi-static process of crack nucleation, propagation and branching is governed by a minimization problem of an energy functional as a function of the displacement field and the crack surface. The minimization of this functional results in a set of admissible cracks and displacement fields on the material. Nonetheless, this problem is rather cumbersome to be tackled since the crack surface is not known a *priori*. Driven by this issue, the phase field approximation emerged, which regularizes the variational formulation, i.e., overcomes the crack discontinuity, and thus eases the numerical implementation of the problem. The regularization, initially presented in [51] for image segmentation, was applied by [52] to fracture in brittle materials. This regularization replaces the use of the crack surface as a variable by a continuous scalar field, called crack phase field, which interpolates continuously and smoothly between the state of intact material and the state of fully damaged material. Such an approximation regularizes the topology of a crack surface through the so-called crack surface density function, governed by the new variable set by a regularization parameter responsible for controlling the width of the damaged region.

Lately, good headway is being made on developing, implementing and analysing methods for brittle fracture for solid shells [53], fibre composites [54,55], and for surfaces with complex geometry and topology [56]. Nevertheless, fewer studies are exploiting numerical models on TPMS structures (see for example [57–59]).

Inspired from the previous studies and results above mentioned, it is suffice to say that robust breakthrough relationships between TPMS cell geometries and their numerical performances from phase field theory must be established. Thus, the main objective towards this endeavour is modelling fracture over TPMS by means of phase field (see [52,60,61]), providing so a powerful framework to characterize and estimate the evolution of damage caused by the crack propagation over TPMS topologies. A consistent quasi-static uniaxial compressive Phase Field finite element model using spectral decomposition of the strain tensor has been developed and implemented on the open-source software FEniCS [62]. CAE-CAD models of TPMS are designed by the software developed at the University of Nottingham, FlattPack, in order to use them as input to phase field simulations. Throughout, a mesh sensitivity analysis is conducted over the unit cells of the following TPMS geometries: Primitive, Gyroid, IWP, Diamond and Neovius. Ultimate compressive stresses and the apparent Young's moduli in compression are calculated via the stress–strain curves predicted by the phase field simulations. The estimated mechanical properties of the five types of TPMS, for different volume fractions, are reported on Ashby charts [34,63,64], describing the relationship among them. Moreover, they are compared with those of open cell aluminium alloy foams available in the literature, in order to provide a better understanding of how the damage pattern correlates to the TPMS geometry and their aforementioned mechanical properties, giving also quantitative indications to materials scientists for further research and applications of TPMS in different fields.

## 2. Methodology and theoretical framework

### 2.1. Mathematical characterization of TPMS structures

Beyond the classical definition of a vanishing mean curvature, there is a plethora of different ways, yet equivalent, to define minimal surfaces, and therefore TPMS. Notwithstanding, triply periodic minimal surfaces can be precisely defined by the

Weierstrass–Enneper representation [2], as in the following: let $w = u + iv$ be the complex variable defined on a open set $\mathcal{D} \in \mathbb{C}$, thus the Weierstrass–Enneper parametrization is

$$\begin{aligned} x(w) &= \Re e\left(\int_{w_0}^{w} e^{i\theta}(1-\tau^2)R(\tau)d\tau\right), \\ y(w) &= \Re e\left(\int_{w_0}^{w} e^{i\theta} i(1-\tau^2)R(\tau)d\tau\right), \\ z(w) &= \Re e\left(\int_{w_0}^{w} e^{i\theta} 2\tau R(\tau)d\tau\right), \end{aligned} \tag{1}$$

where $R(\tau)$ (Weierstrass function) is a non vanishing analytic function defined on a simply connected domain in $\mathbb{C}$, and the multiplication by a complex number of unit magnitude is known as the Bonnet transformation by the Bonnet angle $\theta$ [65], which has been an useful tool in generating new TPMS by converting the free boundary problem to the Plateau's problem [66–68]. The minimal surfaces are determined by integrating the coordinates in Eq. (1), which analytical solutions constructed by reflection or rotation (through the Bonnet angle) about the patch boundary entirely generates the surface for some TPMS [69–71]. Nonetheless, in practice, computing the complex integrals using Weierstrass–Enneper representation (1) can be rather worrisome to be tackled, and by consequence evaluate their effective properties.

As matter of fact, once the TPMS are characterized for its periodicity in the three independent Cartesian directions, such surfaces can be approximated by the periodic nodal surfaces (PNS) of a sum defined in terms of the Fourier series [13,72,73],

$$\Psi(\boldsymbol{r}) = \sum_{\mathbf{k}} F(\mathbf{k}) \cos[\mathbf{k}\cdot\boldsymbol{r} - \alpha(\mathbf{k})] = C, \tag{2}$$

where $\boldsymbol{r} \in \mathbb{D} \subset \mathbb{R}^3$, $\mathbb{D}$ a closed set dependent of $\mathbf{k}$, which are the TPMS function periodicities, $\alpha(\mathbf{k})$ is a phase shift, and the structure factor $F(\mathbf{k})$ is an amplitude associated with a given $\mathbf{k}-$vector. Naturally, the quality of the approximation of a TPMS by nodal surfaces depends on the number of terms in the Fourier series (2). However, the minimal surface is satisfactorily reproduced by truncating such series to the leading point and setting the level surface $C = 0$, where the resulting minimal surface will split the space into two sub-domains of equal volumes [74,75]. For a nodal surface described by the Eq. (2), the mean curvature and the Gaussian curvature are given in terms of the unit normal vector field $\mathbf{n}$ [75,76], respectively, as

$$\mathrm{H} = \nabla\cdot\mathbf{n}, \tag{3}$$

$$\mathrm{K} = \frac{\mathbf{n}\cdot\nabla^2\mathbf{n} + [\nabla\cdot\mathbf{n}]^2 + [\nabla\times\mathbf{n}]^2}{2}, \tag{4}$$

with $\mathbf{n} = \nabla\Psi(\boldsymbol{r})/\|\nabla\Psi(\boldsymbol{r})\|$.

In the present work, the decision of taking a specific definition among all relies on how the mathematical description of the surface will unravel the analytical, numerical and experimental steps. It is noteworthy that although representing the TPMS through a truncation of the Fourier series (2) does not give a surface with an exact zero mean curvature in Eq. (3), the viability is quite simple and accessible [73,74,77], once the truncated series to the leading term give rise to an implicit function (as known as isosurface) essentially formed of a combination of trigonometric functions. Such an approach has been capable of producing several numerical studies in the area of mechanics showing the multi-functionality of the TPMS [14,78,79], their mechanical properties by means of finite elements analysis (FEA) [57,80], and additive manufactured TPMS prototypes [17,19,25,26,44,59], as well as in tissue engineering via AM in order to predict experimentally, with the aid of FEA, responses of cellular TPMS models [21,22,27,81,82].

### 2.2. Phase field approach to fracture: variational formulation

Let us consider an arbitrary $n$-dimensional solid body $\Omega$ in the Euclidean space $\mathbb{R}^n$, with its external boundary $\partial\Omega \in \mathbb{R}^{n-1}$, in which an evolving internal discontinuity $\Gamma \in \mathbb{R}^{n-1}$ is postulated. The position of a material point is denoted by the vector $\mathbf{x}$ in the global Cartesian frame within the bulk. The body is characterized by the kinematic displacement field $\mathbf{u}(\mathbf{x})$ and the strain field is defined as a symmetric gradient $(\nabla^s(\cdot))$ of the displacement field, i.e. $\boldsymbol{\epsilon}(\mathbf{x}) := \nabla^s(\mathbf{u}(\mathbf{x}))$ for all $\mathbf{x} \in \Omega$. The external boundary of the body $\partial\Omega \in \mathbb{R}^{n-1}$ is split into two disjoint sets, namely $\partial\Omega_{\mathbf{u}} \subset \partial\Omega$ and $\partial\Omega_{\mathbf{t}} \subset \partial\Omega$, with $\overline{\partial\Omega_t \cup \partial\Omega_{\mathbf{u}}} = \partial\Omega$ and $\partial\Omega_{\mathbf{t}} \cap \partial\Omega_{\mathbf{u}} = \emptyset$, such that the displacement boundary conditions are prescribed as $\bar{\mathbf{u}}(\mathbf{x})$ for $\mathbf{x} \in \partial\Omega_{\mathbf{u}}$, and traction conditions are given by $\boldsymbol{\sigma}\cdot\mathbf{n} = \bar{\mathbf{t}}(\mathbf{x})$ for $\mathbf{x} \in \partial\Omega_{\mathbf{t}}$, where $\mathbf{n}$ denotes the outward normal unit vector to the body, and $\boldsymbol{\sigma}$ is the Cauchy stress tensor, as shown in Fig. 1(a). Therefore, the external potential energy functional is defined by

$$\Pi_{\mathrm{ext}}(\mathbf{u}) = \int_{\partial\Omega} \bar{\mathbf{t}}\cdot\mathbf{u}\ \mathrm{dS} + \int_{\Omega} \mathbf{b}\cdot\mathbf{u}\ \mathrm{dV}, \tag{5}$$

where $\mathbf{b} : \Omega \longrightarrow \mathbb{R}^n$ is the distributed body force.

The variational approach to fracture governing crack nucleation, propagation and branching according to Griffith's theory [83–85] is set up through the definition of the following total energy functional [61,84,86] in a quasi-elastic loading regime

$$\Pi(\mathbf{u},\Gamma) = \Pi_{\Omega}(\mathbf{u},\Gamma) + \Pi_{\Gamma}(\Gamma) + \Pi_{\mathrm{ext}}(\mathbf{u}), \tag{6}$$

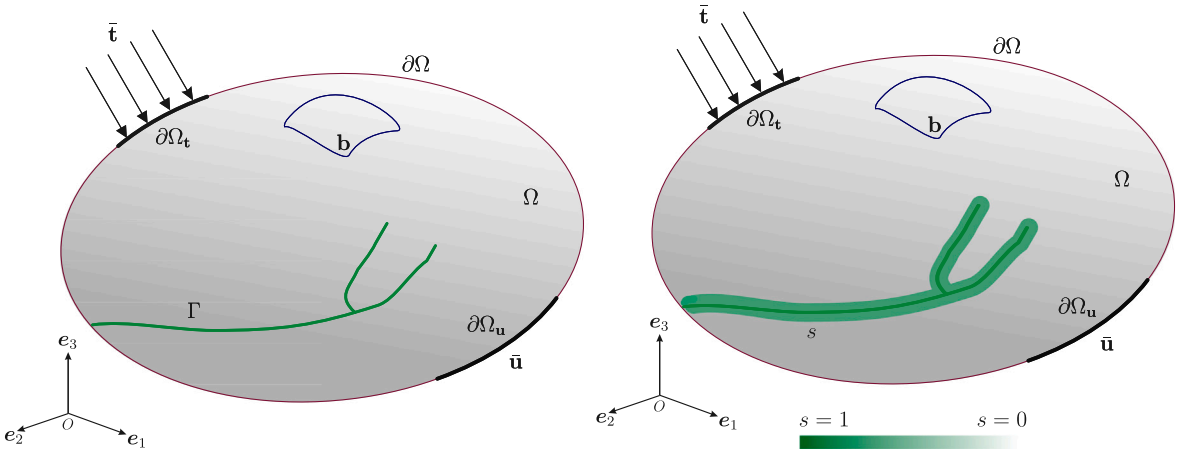


(a) Sharp crack in the bulk. (b) Phase field regularization.

**Fig. 1.** Schematic illustration of diffusive cracks.

where $\Pi_{\Omega}(\mathbf{u}, \Gamma)$ identifies the elastic energy stored in the damaged body given by a volume integral, while the energy required to create the crack complying with the Griffith criterion is denoted by $\Pi_{\Gamma}(\Gamma)$ given by a surface integral. Therefore, the total energy functional (6) reads

$$\Pi(\mathbf{u}, \Gamma) = \int_{\Omega \setminus \Gamma} \psi^e(\boldsymbol{\varepsilon}) \, \mathrm{dV} + \int_{\Gamma} \mathcal{G}_c \mathrm{dS} + \Pi_{\mathrm{ext}}(\mathbf{u}), \tag{7}$$

where $\psi^e(\boldsymbol{\varepsilon})$ is the elastic energy density function that depends upon the strain field $\boldsymbol{\varepsilon}(\mathbf{u})$, and $\mathcal{G}_c$ is the fracture energy. In this scenario, at any given pseudo-time step $t \in [0, T]$, minimizing the functional (7) results in a crack set $\Gamma_t \subset \Omega$ ($\Gamma_t \supset \Gamma_t$), and a quasi-static displacement field $\mathbf{u}^t : \Omega \longrightarrow \mathbb{R}^n$, which is discontinuous over $\Gamma_t$. However, the path to solve this problem is very tortuous since the crack surface $\Gamma$ is unknown a *priori* [50,52].

To regularize the problem, i.e. the replacement of the crack surface variable by the phase field variable, introduces a smooth continuous scalar field damage function $s(\mathbf{x}, t)$ with $s \in [0, 1]$, [51,52,84], where $s = 0$ represents an intact material, and $s = 1$ identifies the fully damaged state (see Fig. 1(b)). Hence, the dissipated surface energy associated with the crack in the bulk $\Omega$ is approximated by

$$\Pi_{\Gamma} = \int_{\Gamma} \mathcal{G}_c(\mathbf{x}, s) \mathrm{dS} \cong \int_{\Omega} \mathcal{G}_c \gamma^l(s, \nabla s) \, \mathrm{dV}. \tag{8}$$

where $\gamma^l(s, \nabla s)$ stands for the so-called crack surface energy density function. According to [61], the function $\gamma^l(s, \nabla s)$ is given by

$$\gamma^l(s, \nabla s) = \frac{1}{2l} s^2 + \frac{l}{2} |\nabla s|^2, \tag{9}$$

where $l \in \mathbb{R}^+$ stands for a regularization parameter related to the smeared crack width, responsible for controlling the width of the transition zone of the regularized crack. Thus, when the characteristic regularization parameter tends to zero ($l \to 0$), then the formulation outlined in Eq. (8) tends to its respective term in Eq. (6) in the sense of the so-called $\Gamma$-convergence [60,87,88].

In what regards the dependency of the energy density of the bulk $\psi(\boldsymbol{\varepsilon}, s)$ in Eq. (7), due to the regularization of the crack $\Gamma$ by the phase field variable $s$, it also becomes $s(\mathbf{x})$ dependent, which means that

$$\psi^e(\mathbf{u}, s) = g(s)\psi_+(\boldsymbol{\varepsilon}(\mathbf{u})) + \psi_-(\boldsymbol{\varepsilon}(\mathbf{u})), \tag{10}$$

where $g(s)$ is a monotonically decreasing function representing the energetic degradation function characterized by the initial elastic energy function, such that $g(s) = (1 - s)^2 + k_l$, with $k_l = \mathcal{O}(l) > 0$ a parameter that defines a residual stiffness to prevent numerical instabilities in the computational implementation, and simultaneously preventing that the resulting system of equations becomes ill-conditioned and $\psi_{\pm}$ the tensile and compressive part of the strain energy density as defined in [61]. Note that, since the phase field variable $s$ is bounded, the degradation function chosen $g(s) = (1 - s)^2$ [52] is bounded as well, mapping $g(s) : [0, 1] \to [1, 0]$. Besides, it satisfies the phase field conditions accordingly to Griffith' theory and modifications.

Based on the previous regularizing assumptions within the framework of the phase field approach [52,61,84], the potential energy of the system in Eq. (6) can be recast as

$$\Pi_l(\mathbf{u}, s) = \int_{\Omega} [(1 - s)^2 + k_l]\psi_+(\boldsymbol{\varepsilon}(\mathbf{u})) + \psi_-(\boldsymbol{\varepsilon}(\mathbf{u})) \, \mathrm{dV} + \int_{\Omega} \frac{\mathcal{G}_c}{2} \left[ \frac{s^2}{l} + l |\nabla s|^2 \right] \mathrm{dV} + \Pi_{\mathrm{ext}}(\mathbf{u}). \tag{11}$$

with $\mathbf{u}, s \in \mathrm{H}^1(\Omega)$, accordingly to [51].

A standard derivation [52,61,84] leads Eq. (10) to the Cauchy stress tensor from the strain energy density,

$$\boldsymbol{\sigma}(\mathbf{u},s)=g(s)\boldsymbol{\sigma}_{+}+\boldsymbol{\sigma}_{-}=g(s)\frac{\partial\psi_{+}(\boldsymbol{\varepsilon})}{\partial\boldsymbol{\varepsilon}}+\frac{\partial\psi_{-}(\boldsymbol{\varepsilon})}{\partial\boldsymbol{\varepsilon}}\ . \tag{12}$$

The weak form corresponding to the phase field model for brittle fracture can be derived following a standard Galerkin procedure. In particular, the weak form of the coupled displacement and phase field damage problem according to Eq. (11) [61] is,

$$\delta\Pi_{l}=\int_{\Omega}\boldsymbol{\sigma}(\mathbf{u}):\boldsymbol{\varepsilon}(\mathbf{v})\mathrm{d}\mathbf{V}-\int_{\Omega}2H_{+}(\boldsymbol{\varepsilon})(1-s)\phi\ \mathrm{d}\mathbf{V}+\int_{\Omega}\mathcal{G}_{c}\left\{\frac{s\phi}{l}+l\nabla s\cdot\nabla\phi\right\}\mathrm{d}\mathbf{V}+\delta\Pi_{\mathrm{ext}}, \tag{13}$$

where $H_{+}(\boldsymbol{\varepsilon})=\max_{\tau\in[0,t]}\left\{\psi_{+}^{e}(\boldsymbol{\varepsilon}(\tau))\right\}$ is the strain history function, accounting for the irreversibility of crack formation [61], $\mathbf{v}$ is the vector of the displacement test functions defined on $\mathbf{H}_{0}^{1}(\Omega)$, $\phi$ stands for the phase field test function defined on $\mathbf{H}_{0}^{1}(\Omega)$. Eq. (13) holds for every test functions $\mathbf{v}$ and $\phi$. The external contribution to the variation of the bulk functional in Eq. (13) is defined as follows

$$\delta\Pi_{\mathrm{ext}}(\mathbf{u},\mathbf{v})=\int_{\partial\Omega_{\mathbf{t}}}\bar{\mathbf{t}}\cdot\mathbf{v}\ \mathrm{d}\mathbf{S}+\int_{\Omega}\mathbf{b}\cdot\mathbf{v}\ \mathrm{d}\mathbf{V}. \tag{14}$$

Given the prescribed loading condition $\bar{\mathbf{u}}_{n}$ and $\bar{\mathbf{t}}_{n}$ at step $n$, the mechanical problem can be stated as finding $\mathbf{u}\in\mathbf{U}=\left\{\mathbf{u}\,|\,\mathbf{u}=\bar{\mathbf{u}}_{n}\ \text{on}\ \partial\Omega_{u},\mathbf{u}\in\mathbf{H}^{1}(\Omega)\right\}$, such that

$$\int_{\Omega}\boldsymbol{\sigma}(\mathbf{u}):\boldsymbol{\varepsilon}(\mathbf{v})\mathrm{d}\mathbf{V}-\int_{\partial\Omega}\bar{\mathbf{t}}\cdot\mathbf{v}\mathrm{d}\mathbf{S}-\int_{\Omega}\mathbf{b}\cdot\mathbf{v}\mathrm{d}\mathbf{V}=0,\quad\forall\mathbf{v}\in\mathbf{H}_{0}^{1}(\Omega), \tag{15}$$

while the phase field problem is formulated by finding $s\in S=\left\{s\,|\,s=0\ \text{on}\ \Gamma,s\in\mathbf{H}^{1}(\Omega)\right\}$ such that $\forall\phi\in\mathbf{H}_{0}^{1}(\Omega)$, gives

$$\int_{\Omega}\mathcal{G}_{c}l\nabla s\cdot\nabla\phi\mathrm{d}\mathbf{V}+\int_{\Omega}\left(\frac{\mathcal{G}_{c}}{l}+2H_{+}\right)s\phi\mathrm{d}\mathbf{V}-\int_{\Omega}2H_{+}\phi\mathrm{d}\mathbf{V}=0. \tag{16}$$

To solve the quasi-static evolution problem for brittle fracture, isoparametric linear triangular finite elements are used for the spatial discretization, and a staggered solution scheme is considered. Staggered schemes based on alternate minimization exploit the convexity of the energy functional with respect to each individual variable $\mathbf{u}$ and $s$.

At this stage, it is fundamental to remark that, in order to predict crack trajectories in TPMS unit cell open foams under tensile/compressive stress states, the phase field finite element method was formulated by decomposing the strain energy density $\psi^{e}(\mathbf{u},s)$ in Eq. (10), based on the spectral diagonalization according to [61], in active and passive parts, in order to apply the degradation of the material response only in tension. The variational formulation is then implemented on FEniCS [62] environment, see also [89] for more details.

The length scale $l$ is deeply inserted for modelling phase field, considering that for a sufficiently small length scale $l_{0}$, the functional (11) converges to the total potential energy functional (6), in the sense that the global minimizers of $\Pi_{l}$ will also converge to that of $\Pi$. This entails that the length scale must be carefully chosen, rather than setting it arbitrarily. In the context of the uniaxial tension of a homogeneous bar, the length scale $l$ was experimentally determined in [86,90–92], and well summarized in [93]. Thereby, the length scale $l$ value is linked to the apparent material strength. Particularly, as proposed in [94], once these material properties such as Young's modulus $E$, critical energy release rate $\mathcal{G}_{c}$ are known, then the characteristic length $l$ can be set as

$$l=\frac{27}{256}\left(\frac{\mathcal{G}_{c}E}{\sigma_{\max}^{2}}\right). \tag{17}$$

The failure stress $\sigma_{\max}$ can either be obtained by using the closed-form relation $\sigma_{\max}=\sqrt{\mathcal{G}_{c}E/L}$ where $L$ is the characteristic size of the specimen, or obtained through tensile tests, and afterwards the length scale $l$ can be evaluated through Eq. (17).

### 2.3. Modelling TPMS in FEM

In order to apply the phase field scheme to the TPMS lattices, the computer-aided design (CAD) modelling is performed assuming the approximated isosurface established by the truncation of the Fourier series (2) to generate unit cells of the TPMS topologies. Using the software developed at the University of Nottingham, namely FLatt-Pack [95], printable triangular mesh struts spatially discretized by the parameter $\mu$, are then generated as STL files by offsetting $(-C\leq\Psi(x,y,z)\leq C)$ the minimal surface controllable by its volume fraction (or relative density) $\rho^{*}=V_{latt}/V$ of the lattice, which is the ratio between the inner volume of the TPMS unit open cell lattice $V_{latt}$ and the enclosing cubic unit open cell volume $V$, controllable by the level set $C$. The spatial discretization factor $\mu$ divides the cell size $L$ into $\mu$ elements of size $L/\mu$, in each direction. The relationship between the volume fraction of the TPMS cell $\rho^{*}$ and the level set $C$ can be seen in [19,96,97]. Usually, the level set $C$ indicates an offset of the surface in the normal direction and/or in the opposite direction to vary the volume fraction $\rho^{*}$ at each TPMS lattice type.

Additionally, before importing them to the finite element environment FEniCS, uniform tetrahedral meshes are constructed by transferring the STL triangular meshes into the pre-processing software HyperMesh [98], producing the necessary tetrahedral solid assessed and converted to MSH file by Gmsh software [99]. As stated in [100], it is recommended that uniform meshes should be used for phase field models, in particular for brittle fracture simulation. Even though 3D continuum tetrahedral-like meshes might present less accuracy over the edges of the surface when a phase field finite element technique is playing a role (contact problems

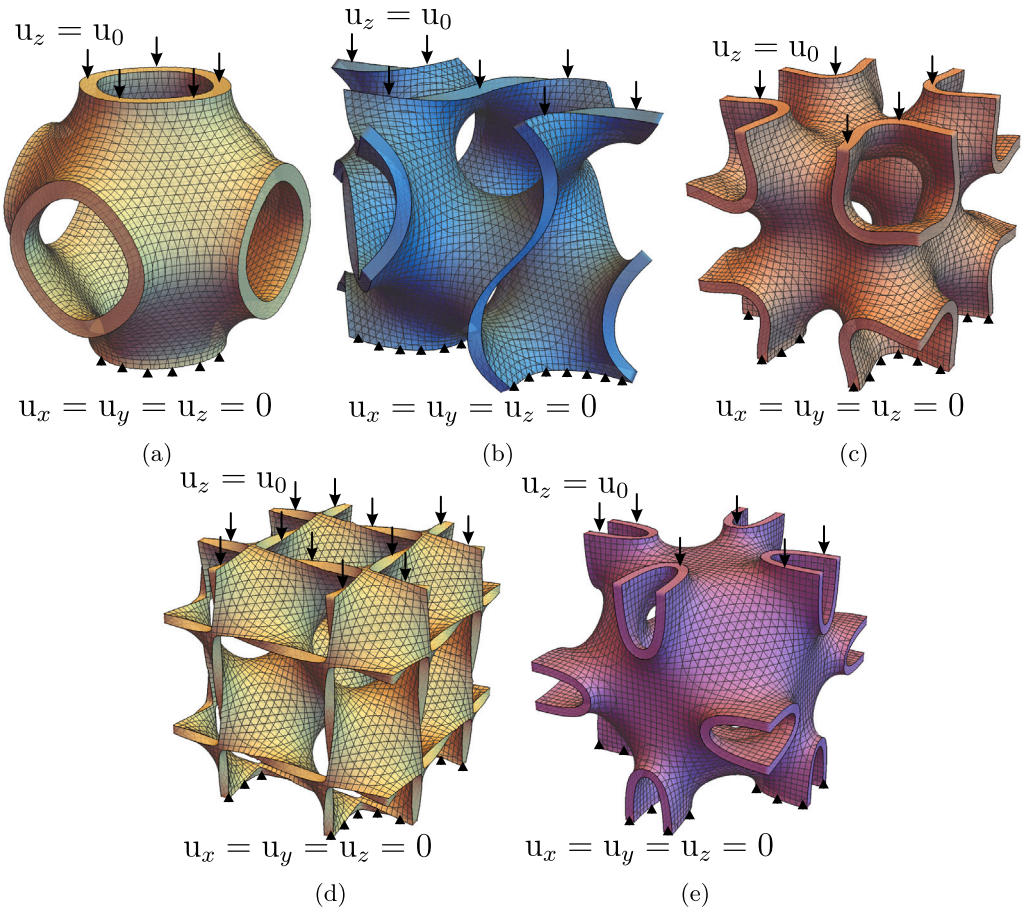


**Fig. 2.** Unit cells of TPMS structures, boundary conditions and applied uniaxial load: (a) Schwarz Primitive; (b) Schoen Gyroid; (c) Schoen-I-WP; (d) Schwarz Diamond; (e) Neovius.

for instance [101,102]), the choice of working with them rather than using hexahedral solid shells is based on the complexity that the topology of a TPMS type may take, thus facilitating the representation of the surface curvatures more accurately [39,103–105].

The TPMS types chosen to have the phase field scheme applied are the Schwarz Primitive (P) (Fig. 2(a)), Schoen Gyroid (G) (Fig. 2(b)), Schoen-I-WP (IWP) (Fig. 2(c)), Schwarz Diamond (D) (Fig. 2(d)) and Neovius (N) (Fig. 2(e)) expressed as isosurfaces, respectively, as

$$\Psi_{\mathrm{P}}(x,y,z) = \cos(\mathrm{k}_x x) + \cos(\mathrm{k}_y y) + \cos(\mathrm{k}_z z) - C, \tag{18a}$$

$$\Psi_{\mathrm{G}}(x,y,z) = \cos(\mathrm{k}_x x)\sin(\mathrm{k}_y y) + \cos(\mathrm{k}_y y)\sin(\mathrm{k}_z z) + \cos(\mathrm{k}_z z)\sin(\mathrm{k}_x x) - C, \tag{18b}$$

$$\Psi_{\mathrm{IWP}}(x,y,z) = 2(\cos(\mathrm{k}_x x)\cos(\mathrm{k}_y y) + \cos(\mathrm{k}_y y)\cos(\mathrm{k}_z z) + \cos(\mathrm{k}_x x)\cos(\mathrm{k}_z z)) - (\cos(2\mathrm{k}_x x) + \cos(2\mathrm{k}_y y) + \cos(2\mathrm{k}_z z)) - C, \tag{18c}$$

$$\Psi_{\mathrm{D}}(x,y,z) = \cos(\mathrm{k}_x x)\cos(\mathrm{k}_y y)\cos(\mathrm{k}_z z) - \sin(\mathrm{k}_x x)\sin(\mathrm{k}_y y)\sin(\mathrm{k}_z z) - C, \tag{18d}$$

$$\Psi_{\mathrm{N}}(x,y,z) = 3(\cos(\mathrm{k}_x x) + \cos(\mathrm{k}_y y) + \cos(\mathrm{k}_z z)) + 4(\cos(\mathrm{k}_x x)\cos(\mathrm{k}_y y)\cos(\mathrm{k}_z z)) - C, \tag{18e}$$

where the periodicity components are $\mathrm{k}_i = 2\pi n_i / L_i$ for each direction $i = x, y, z$, having $n_i$ as the number of cell repetitions, and $L_i$ correspond to the absolute length of the structure.

### 2.4. Boundary conditions for quasi-static uniaxial compressive loading

Let $\mathbf{u}(\mathbf{x}) = (\mathrm{u}_x(\mathbf{x}), \mathrm{u}_y(\mathbf{x}), \mathrm{u}_z(\mathbf{x}))$, with $\mathbf{x} = (x, y, z) \in \partial\Omega$, be the displacement field, and let $\mathrm{u}_0$ be the magnitude of the applied displacement. The brittle fracture phase field, deformation behaviour and mechanical properties of the TPMS structures are investigated under the boundary conditions subjected to an uniaxial compressive loading of the quasi-static phase field model having on the top face $\mathrm{u}_z = \mathrm{u}_0$ in the normal direction together with free $\mathrm{u}_x$, $\mathrm{u}_y$, and $\mathbf{u}$ free on the lateral faces. In order to avoid any rigid body movement, such as slipping, the bottom face has been constrained by $\mathrm{u}_z = 0$, and on a small region of the bottom by $\mathrm{u}_x = \mathrm{u}_y = 0$. Namely, the lateral free boundary condition set up allows the open celled lattices to deform without any

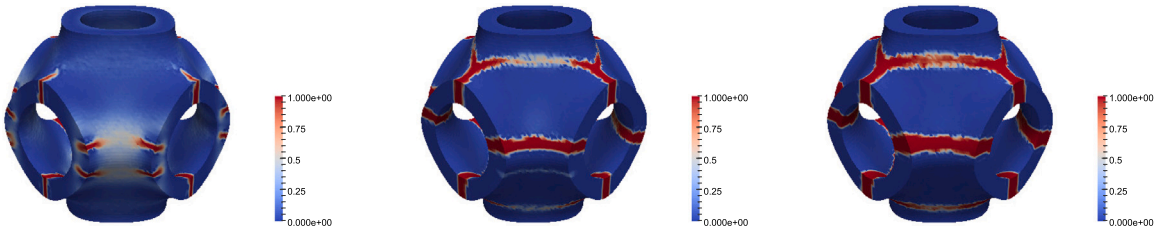


**Fig. 3.** Primitive unit cell crack sites, nucleation, propagation and branching, for 1%, 2%, and 3% of strain.

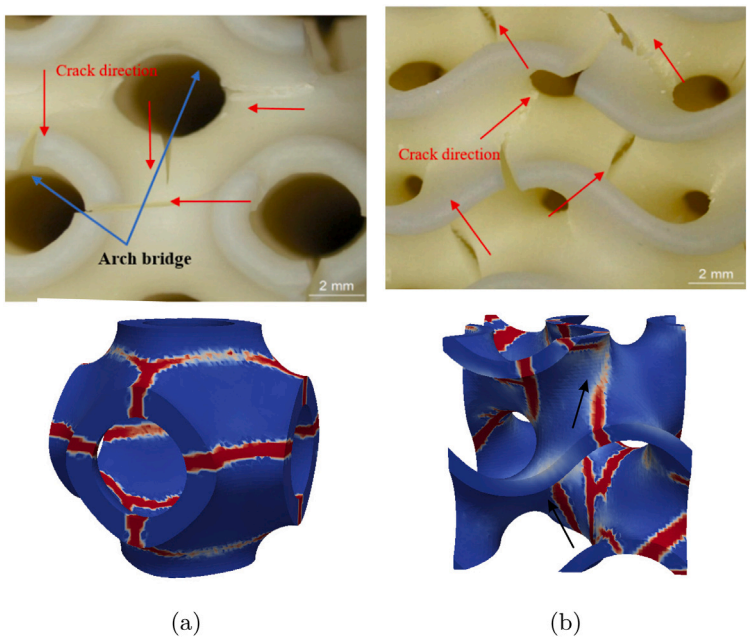


**Fig. 4.** Comparative illustration of the crack pattern in compressive regime derived in [41] (above lattices), and the developed phase field model (below cells). (a) Primitive; (b) Gyroid.

interference due to the absence of neither neighbour cells nor walls. The finite element meshes of all TPMS topologies, with the described boundary conditions, are depicted in Fig. 2.

## 3. Phase field prediction of fracture patterns

Based on the careful mesh sensitivity analysis made in Appendix, the following phase field characterizations of the TPMS unit cells have the spatial discretization corresponding to $\mu = 65$. TPMS parameters and dimensions as well as phase field finite element parameters selected to pursue the following estimations are detailed in Appendix. Crack initiation sites, propagation and nucleation the contour plots of the phase field damage variable in the post-peak regime are shown in the sequence of Figs. 3 to 9 for an increasing level of deformation, for all TPMS analysed. Meanwhile, the deformation behaviour of the TPMS unit cells can be seen in Fig. 10.

Fig. 3 shows cracks appearing in the directions either parallel or perpendicular to the loading of the Primitive strut, with failure occurring under the form of arch bridges, bifurcating to sub-cracks on the top and bottom of the unit cell. Crack formation in the direction to the loading was observed coming from the inside of the unit cell, in agreement with the experimental results derived in [28]. Whereby the cracks in the perpendicular direction nucleate from outside and propagate towards inside. Analogously, the crack pattern over the Primitive unit cell right above described is also in very good agreement with the results obtained in [41] (see Fig. 4(a)). In particular, for the cracks nucleating parallel to the loading direction, they occur after the failure of the hollows, then the arch bridge like semicircular parts were loaded, concentrating the stress in the top of the arch bridge. Some sub-cracks are formed by the propagation of these parallel cracks along the top and bottom of Primitive, as a kind of *crown* like pattern, perpendicular to the loading direction, thereby descried as sub-hollow layers. Interestingly, even though the material utilized in [41] is different from the Aluminium alloy herein considered, the crack pattern is similar. As observed and summarized in [106], in fact, regardless

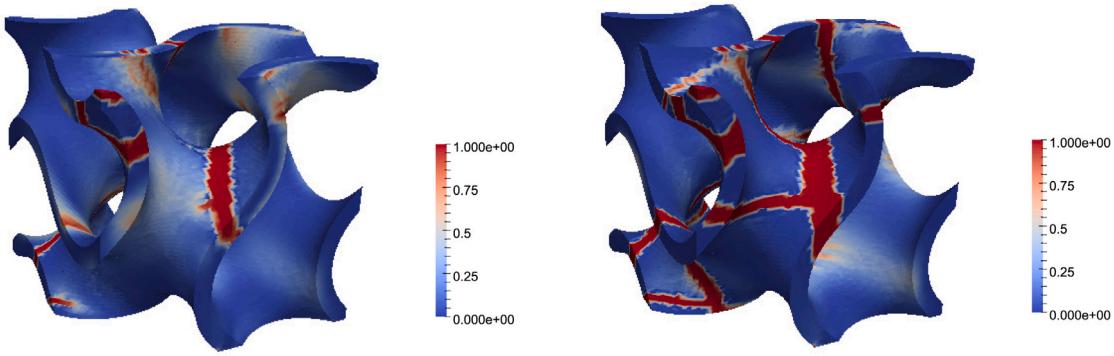


**Fig. 5.** Gyroid unit cell crack sites, nucleation, propagation and branching, for 0.75% and 1.5% of strain.

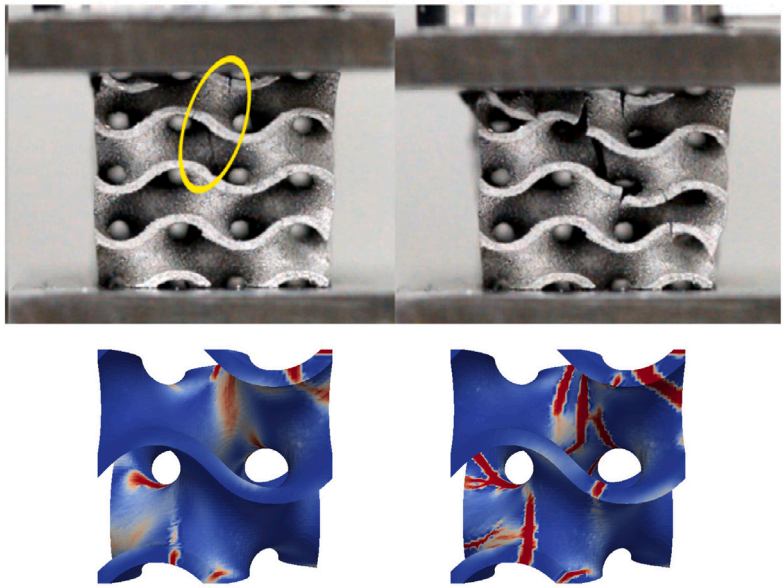

**Fig. 6.** Comparison at low strains between the crack initiation and propagation in the aluminium alloy based Gyroid lattice from experimental tests made in [44], and the present phase field simulated Gyroid unit cell.

of the base material, the topology of the unit cell dictates the stress/strain distribution within the TPMS unit cell under loading regimes, and only post-yield properties depend on the material.

Still in Fig. 3, at a strain of 1%, two horizontal cracks appear and further nucleate at higher strain levels. Based on this scenario, it is conjectured that when fatigue takes place and the lattice collapses, both initial cracks meet, assembling to one branch on the exact deformed/broken spot. The deformation mechanism (see Fig. 10(a)) relates to barrelling behaviour (barrel-shaped), which is in good agreement with previous works [28,34].

For the Gyroid, nucleation, propagation, and branching are shown in Fig. 5, at strains of 0.75% and 1.5%. Cracks are predominantly seen inside of the unit cell, however fractures are also spotted on the boundaries, propagating towards the inside of the cell, resembling a pattern seen in the cluster lattices of the Gyroid in [41]. A contrast of this patterning is shown in Fig. 4(b). Fig. 6 compares the crack initiation and propagation in the aluminium alloy based Gyroid lattice from compressive experimental tests made in [44], against the present phase field model Gyroid unit cell. It can be noted that the phase field crack initiates at in-parts of the unit cell, in agreement with the characterization previously made. As the strain grows, fractures begin to initiate also on the curved band boundaries of the Gyroid. Notwithstanding, the TPMS clusters studied throughout literature are made of ductile material, which may also experience ovalization and instabilities that cannot be predicted from compressive tests on single cells.

IWP phase field characterization is beheld in Fig. 7. The deformation and fracture process of IWP cell shows a dominated expansion on top and bottom of the surface, forming four handles-like, observed in Fig. 10(c) at 1.5% strain. In the upcoming section, it will be remarked that as the volume fraction of IWP cell increases, these handle features become thicker enough to contain this stretching behaviour, letting the deformation stress be dislocated to the mid height region of the strut.

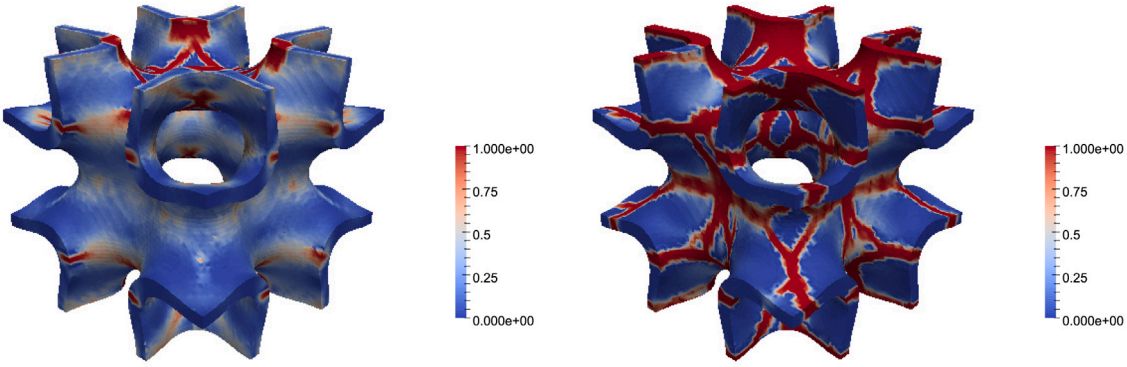


**Fig. 7.** IWP unit cell crack sites, nucleation, propagation and branching, for 0.75% and 1.5% of strain.

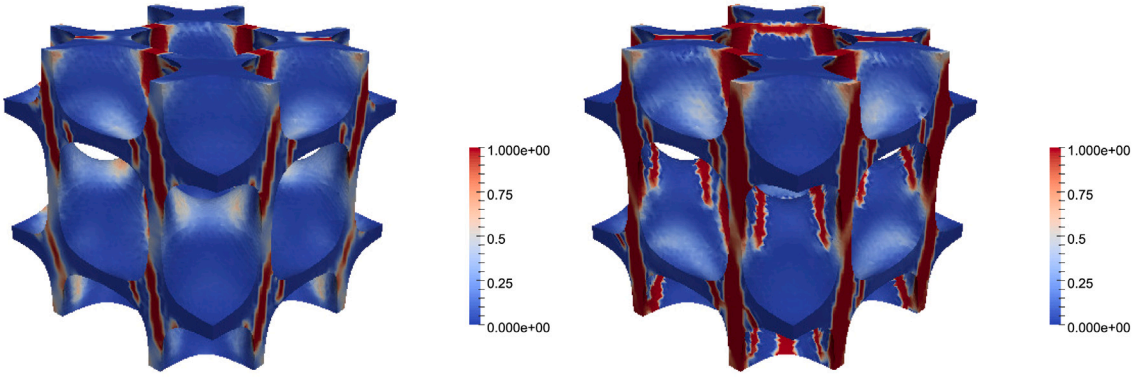


**Fig. 8.** Diamond unit cell crack sites, nucleation, propagation and branching, for 0.88% and 1.75% of strain.

Phase field behaviour of Diamond and Neovius unit cells are depicted at increasing strains of 0.88% and 1.75%, in Figs. 8 and 9, respectively. Diamond phase field is characterized by cracks nucleating with a small inclined angle to the loading direction. as the strain grows, crack initiate over the top of the cell, propagating along the surface curvature perpendicular to the bottom (xy-plane). Cracking on Neovius cells form and evolve in the parallel direction to the loading, secondary cracks nucleate perpendicular to the loading direction when high strain values are reached. A bloating-like deformation behaviour is seen in both Diamond, which is in good agreement with the outcomes seen in [35], and Neovius samples, both depicted at strains of 1.75% in Figs. 10(d) and 10(e).

Notably, during the compression simulations performed, a couple of cracks spread and get connected as the load continues, succeeding in the collapse of the cells and consequently the drop of the stress. Furthermore, the propagation of the cracks within the TPMS lattices exhibit a particular characteristic as consequence of the overall property of self similarity of TPMS. As such, in what regards to the phase field propagation and cell bending, Primitive, IWP, Diamond and Neovius present an uniform pattern led by their geometry design. On the other hand, Gyroid clusters would need to undergo through the phase field scheme to identify and characterize patterns coming from its geometric nature, since a solo unit cell analysed was not sufficient to infer any pattern.

## 4. The effect of the volume fraction on mechanical properties

Guided by the derived numerical results on the mesh sensitivity analysis (see Appendix) for a volume fraction of 20%, the study is herein extended to assess the effect of the volume fraction (or, analogously, the porosity) on the apparent mechanical properties. Here we set the discretization parameter $\mu = 35$ for the Primitive surfaces, $\mu = 40$ for the Gyroid, IWP and Neovius unit cells, while $\mu = 50$ is used for the Diamond lattices. Figs. 11 to 15 depict the TPMS unit cells for different volume fractions.

The volume fraction, which is also related to the porosity as its complement to unity, plays an important role in determining the mechanical properties of porous foams, as typically plotted in Ashby plots [34,63,64]. Here, the quantities of interest for the Ashby plots (apparent Young's modulus, compressive strength, and volume fraction) of lattice TPMS structures are extracted from numerical simulations and examined, see the charts provided in linear (Fig. 16) and bi-logarithmic (Fig. 17) scales.

It is noteworthy that the compressive strength of the open unit cells is an increasing function of the volume fraction. The trend in the stiffness of the TPMS discussed in Appendix for a volume fraction of 20%, is confirmed as the volume fraction increases, i.e. Neovius being the stiffest, followed by IWP, Diamond, Gyroid and Primitive. The same trend occurs for the load carrying capacity in compression, see Fig. 16(a) or 17(a).

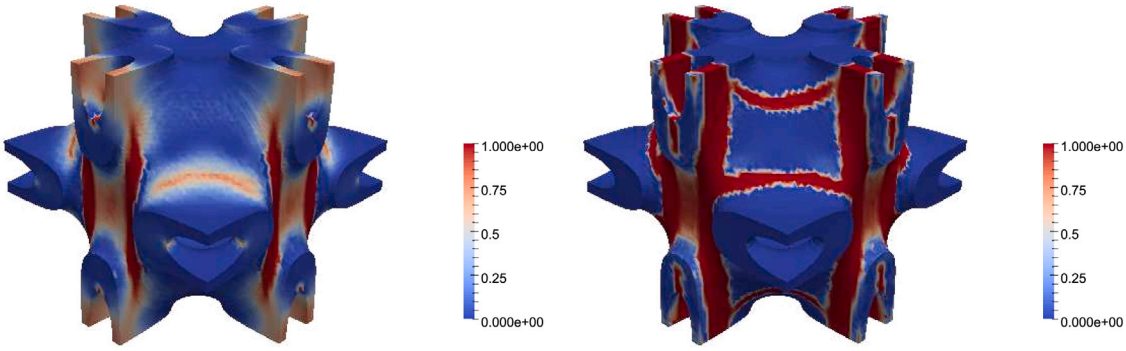


**Fig. 9.** Neovius unit cell crack sites, nucleation, propagation and branching, for 0.88% and 1.75% of strain.

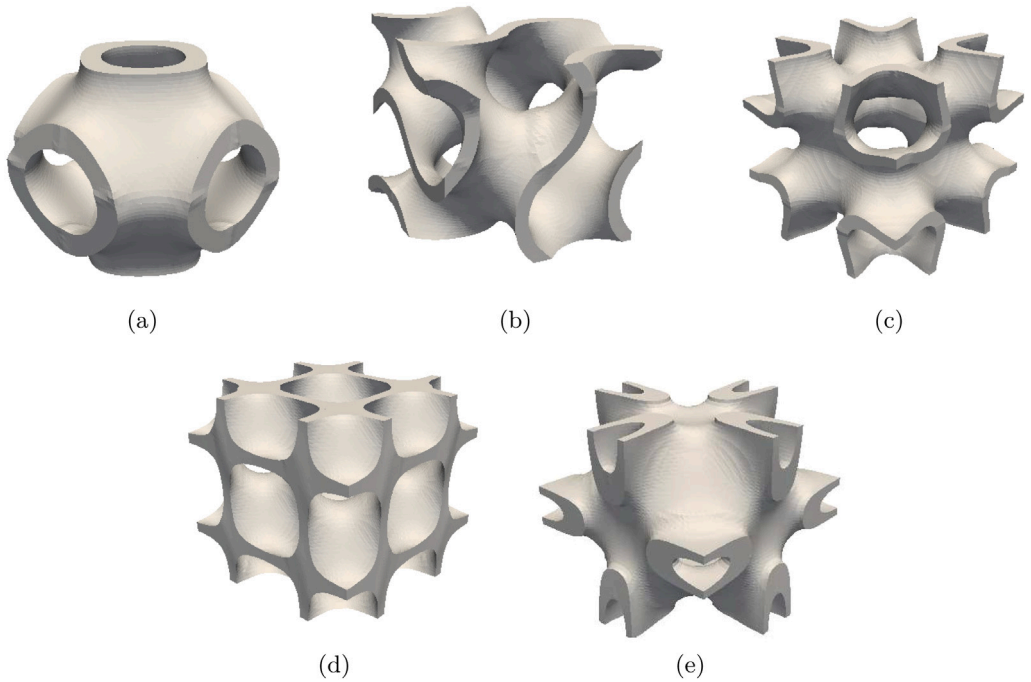


**Fig. 10.** Deformed unit cell TPMS structures at strains of: (a) Schwarz Primitive 3%; (b) Schoen Gyroid 1.5%; (c) Schoen-I-WP 1.5%; (d) Schwarz Diamond 1.75%; (e) Neovius 1.75%.

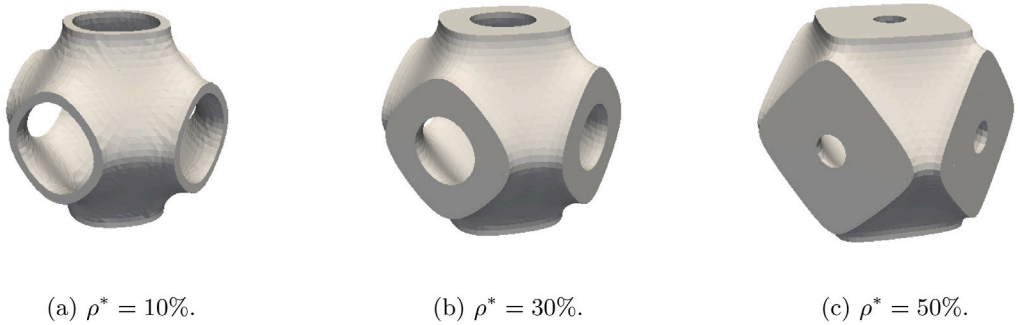


**Fig. 11.** Primitive unit cell at different values of volume fraction.

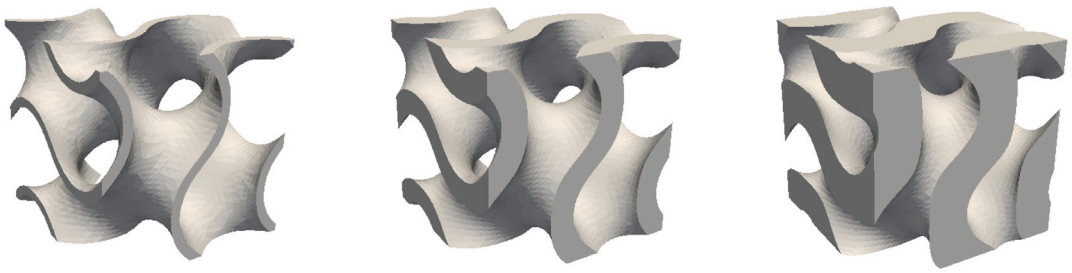

(a) $\rho^* = 15\%$. (b) $\rho^* = 35\%$. (c) $\rho^* = 55\%$.

**Fig. 12.** Gyroid unit cell at different values of volume fraction.

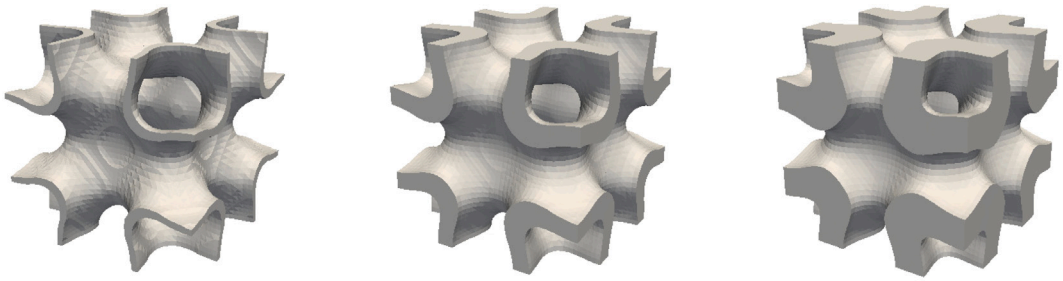

(a) $\rho^* = 15\%$. (b) $\rho^* = 35\%$. (c) $\rho^* = 55\%$.

**Fig. 13.** IWP unit cell at different values of volume fraction.

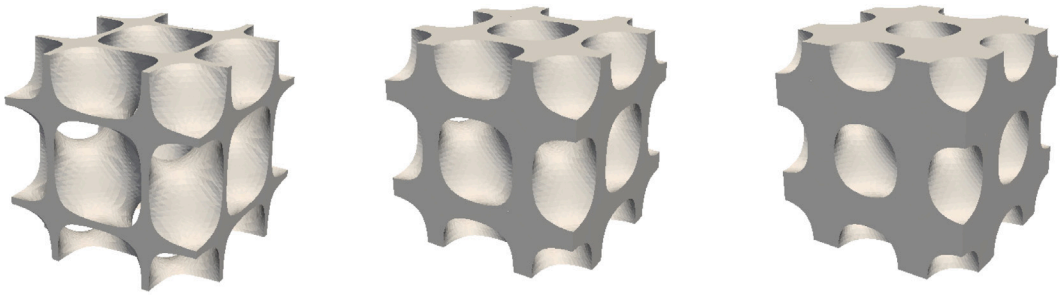

(a) $\rho^* = 15\%$. (b) $\rho^* = 35\%$. (c) $\rho^* = 55\%$.

**Fig. 14.** Diamond unit cell at different values of volume fraction.

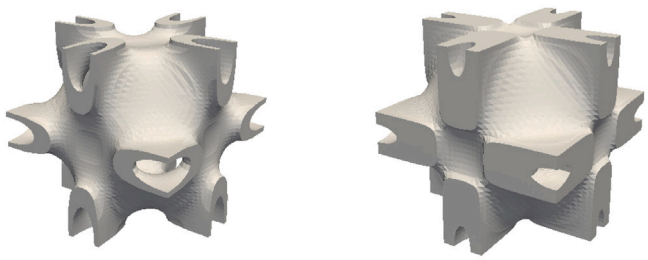

(a) $\rho^* = 15\%$. (b) $\rho^* = 30\%$.

**Fig. 15.** Neovius unit cell at different values of volume fraction.

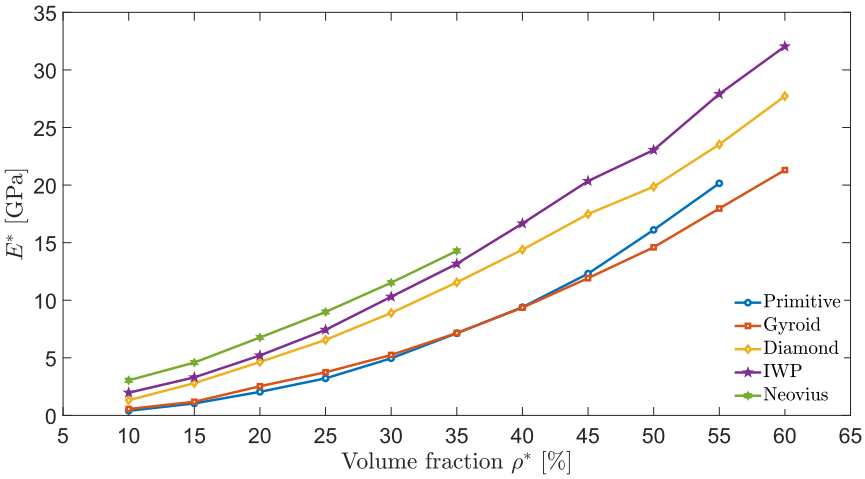


(a) Apparent Young's modulus $E^*$ vs. volume fraction $\rho^*$.

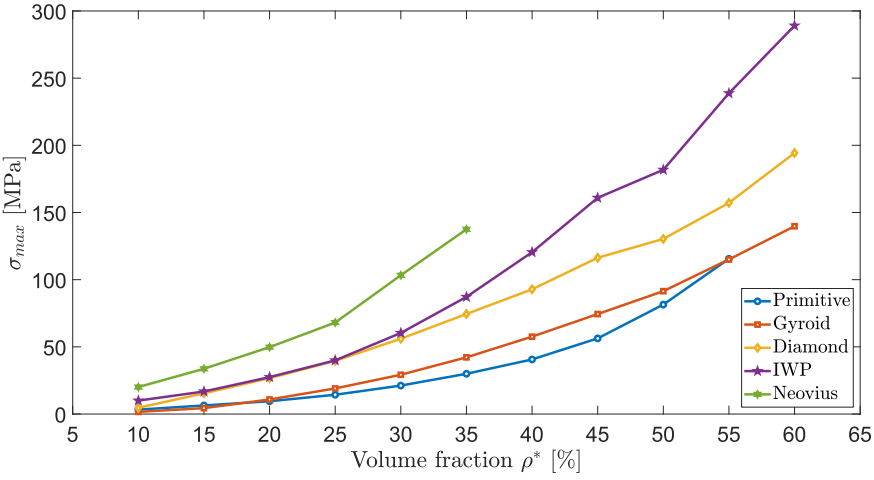


(b) Ultimate compressive stress $\sigma_{\max,c}$ vs. volume fraction $\rho^*$.

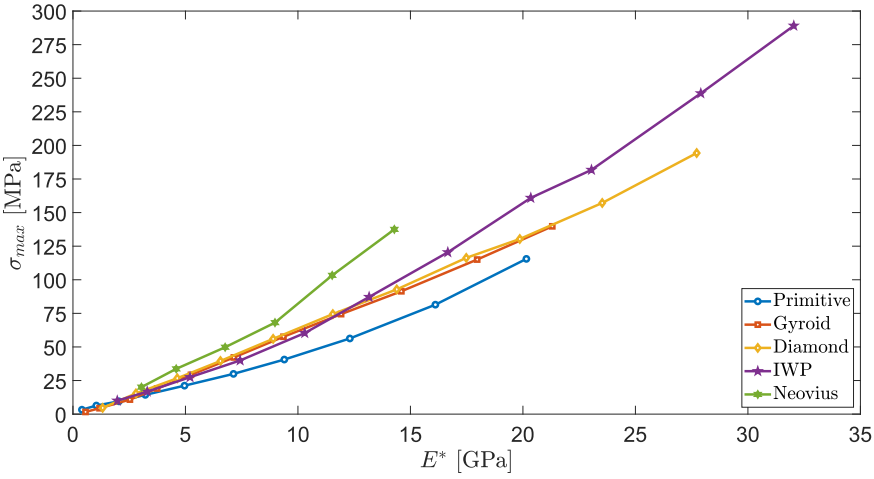


(c) $\sigma_{\max,c}$ vs. $E^*$.

**Fig. 16.** Ashby charts (linear scales).

It can be observed that in between the volume fraction interval of $[35\%, 40\%]$ the Primitive unit cell overtakes the Gyroid unit cell in terms of the apparent Young's modulus $E^*$. Moreover, the results are in reasonable agreement with the findings presented in [40,46], where the latter stated that for low volume fractions, the more relative discrepancy regarding to the elastic properties through the manipulation of the unit cells was found, such a behaviour being clearly evidenced in the bi-logarithmic charts, Figs. 17(a), 17(b) and 17(c). Particularly, Fig. 17(b) shows that, for low volume fractions, the Gyroid cell underperforms all the other TPMS in terms of supported maximum compressive stress $\sigma_{\max,c}$. O the other hand, for higher volume fractions, the less performant TPMS becomes the Primitive one.

In what regards the nucleation sites and deformation for the Primitive cells, the crack initiation sites and their branching seem to happen at the same regions seen in the Primitive at $\rho^* = 20\%$, as the volume fraction increases. Meanwhile, the fracture tips tend to primarily appear at arch bridges of the Primitive geometry, among with barrelling, but uniform, deformation behaviour. From the deformed cells, crumbled regions at the fractured zones perpendicular to the loading are seen, which interconnect the arch bridges of the lateral faces. Interestingly, at lower strains, the cracks initiate firstly and propagate more rapidly for the cells with higher volume fractions. The Primitive with $\rho^* = 55\%$, for instance, is almost entirely crushed, while the Primitive at $\rho^* = 10\%$ resembles the original minimal surface, at mid strain values.

The crack pattern predicted by the phase field model for the Gyroid type unit cells is essentially similar for all the volume fractions, meaning that crack sites formed fairly correspond to the ones described at $\rho^* = 20\%$. However, cracks tend to expand quicker on the Gyroid geometries with higher volume fractions. A stretching deformation behaviour mostly concentrates on the bottom boundary of the Gyroid lattices. The ratio between the surface areas of the stretched deformed bottom and the deformed top, indicates a slightly bigger expanded area on the bottom plan of the open cell.

In Diamond cells, crack nucleation begins on the boundaries of the faces. In this case, cracks originated on the lateral faces initiate angled to loading direction and propagate to the inside of the cells. Subsequently, secondary cracks nucleating on the top of the cells propagate downward parallel to loading, guided by Diamond's surface curvature. On the contrary of what is spotted for the Primitive cells, crack development firstly appears on Diamond lattices at lower volume fractions. Under compressive loading, a uniform expansion of the Diamond unit cells can be noticed in all volume fractions as the strain varies.

IWP struts differ in the cracking pattern as volume fractions varies. Up to $\rho^* = 25\%$, nucleation first appears over top and bottom of the surfaces, propagating parallel to the loading direction. In spite of this trend, IWP cells with volume fraction above 25% show a surrounding crack nucleation at the middle region of the surfaces, perpendicular to the loading direction, which could be relevant for fatigue failure. The compressive deformation behaviour predicted by the phase field model verified that the IWP unit cell lattices have a uniform and smooth stretching deformation perpendicular to the loading at all volume fractions registered, which is in good matching with the finding made in [107].

Phase field characterization and deformation mechanisms of the Neovius cells at increasing volume fraction do not present significant differences from those observed at $\rho^* = 20\%$ in Section 3.

Figs. 18 and 19 compare the TPMS unit cell responses with experimental data from metallic TPMS currently available in the literature [106]. For a certain level set $C$ in Eq. (2), a solid-network (skeleton-network) is defined as being the solid of one of the sub-domains divided by the resulting surface, while the remaining sub-domain is assumed to be a void. Sheet-network is considered to be the thickened resulting minimal surface, as described in Sec. 2.3. Sheet-networks TPMS show improved mechanical properties as compared to solid-networks. As expected, from Fig. 18, over the volume fraction interval studied, the various apparent Young's moduli of the five TPMS unit cells analysed by the present phase field framework lie majorly on the sheet-networks region, represented by the black colour, showing reasonable agreement with the existing experimental compressive works on metallic TPMS lattices.

Despite a bigger overlapping of the regions in Fig. 19, revealing that the superiority of TPMS sheet-networks over solid-networks is less evident when compressive peak stresses are examined, the ultimate compressive stress predicted by the phase field approach lie in good agreement with the experimental data of the metallic TPMS samples. Evidently, although the simulations performed by the phase field numerical model were on single unit cells, the numerical results showed great potential among the studies in the literature.

An open cell foam is comprehended as a porous structure in which its pores are interconnected to each other forming a network scaffold. In this instance, once TPMS based lattices split the three dimensional space into two intertwined domains by their porous topologies, and in the absence of solid cell walls, TPMS are systematically studied as open cellular foams. Therefore, the mechanical properties derived in the previous sections are now compared against the available data concerning compressive quasi-static uniaxial regime on open cell aluminium alloy foams. The major results to be compared with the actual outcomes are taken from the extensive review made in [108].

Fig. 20 shows the structural stiffness values of open cell Aluminium alloy foams, represented by the derived Young's modulus of the equivalent continuum, plotted against the volume fraction. Whereby, the results from the phase field for the Primitive, Gyroid, IWP, Diamond and Neovius are plotted with the data grouped in [108]. It can be noted that, over the comparable range of volume fraction, TPMS foams exhibit considerably superior stiffness increasing with the volume fraction, as compared to the majority of the other existing Aluminium foams. The compressive strength of the various Aluminium alloy foams available in literature and TPMS as a function of volume fraction are presented in Fig. 21. Over the comparable range of volume fraction, the load bearing capacity of the five TPMS specimens studied by the phase field model are higher than the other listed foams, which can indicate superior advantage to be chosen in engineering problems where the load bearing capability plays an important role.

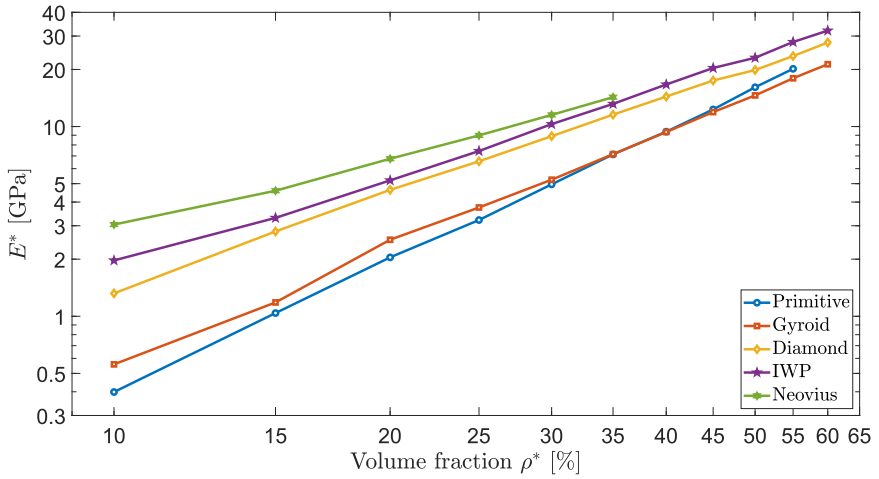


(a) Apparent Young's modulus $E^*$ vs. volume fraction $\rho^*$.

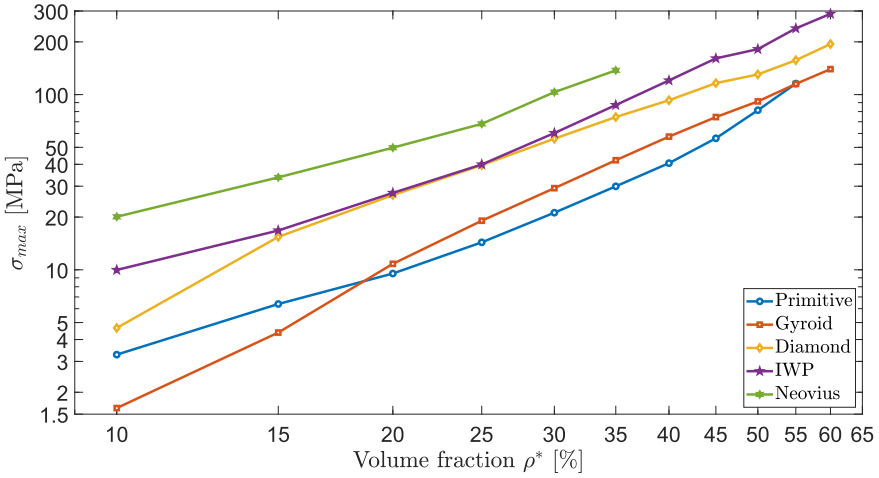


(b) Ultimate compressive stress $\sigma_{\max,c}$ vs. volume fraction $\rho^*$.

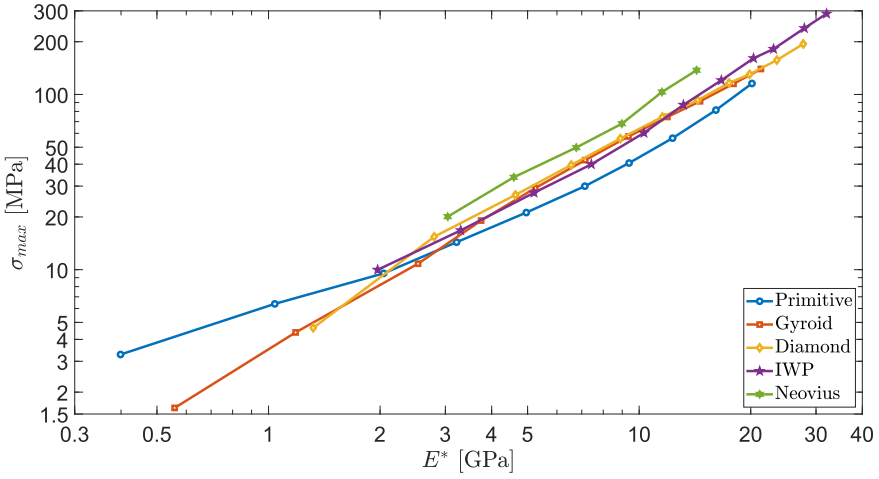


(c) $\sigma_{\max,c}$ vs. $E^*$.

**Fig. 17.** Ashby charts (bi-logarithmic scales).

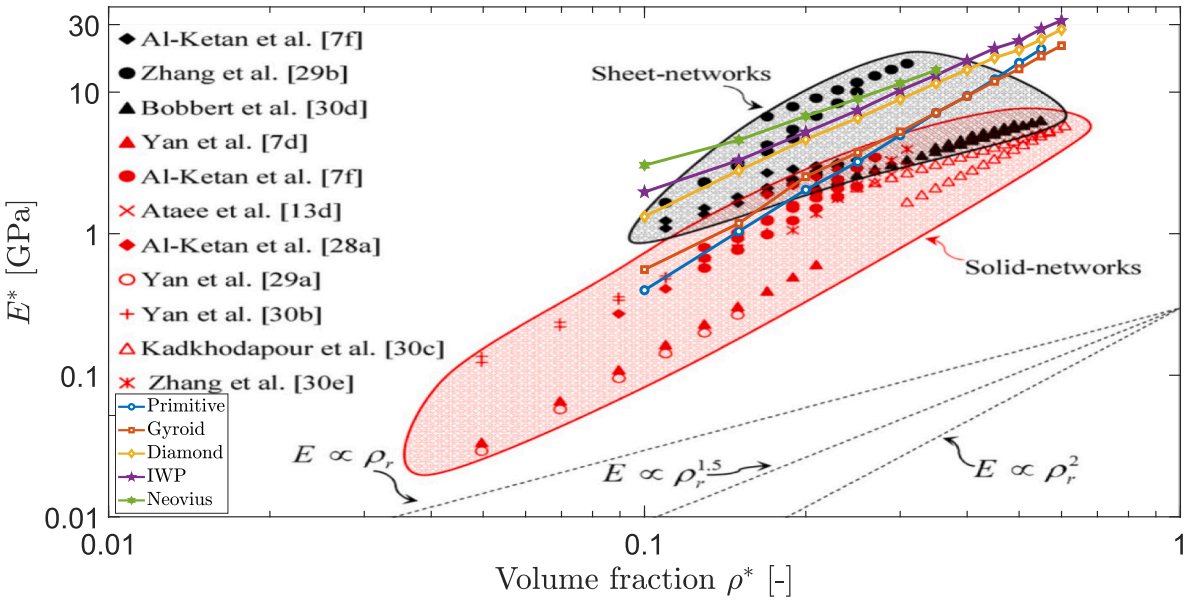


**Fig. 18.** Ashby bi-logarithmic diagram comparing the numerically predicted Young's modulus $E^*$ vs. volume fraction $\rho^*$ of the tested TPMS, with experimental data from metallic TPMS [106]. For details in the legends please see references in Fig. 17(a) in [106].

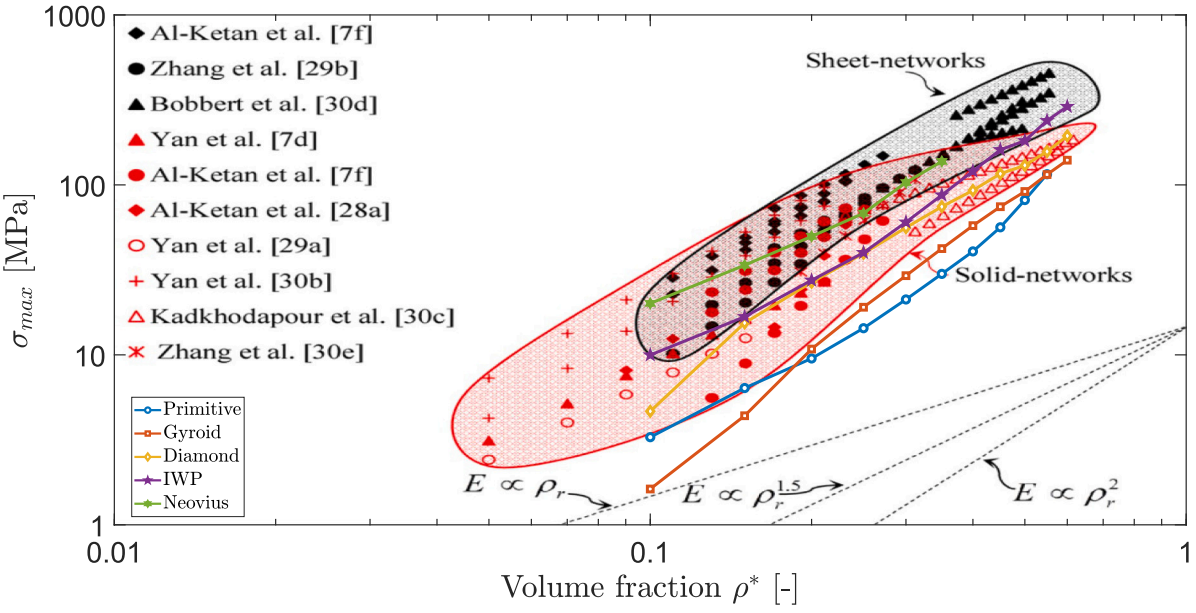


**Fig. 19.** Ashby bi-logarithmic diagram comparing the numerically predicted ultimate compressive stress $\sigma_{max,c}$ vs. volume fraction $\rho^*$ of the tested TPMS, with experimental data from metallic TPMS [106]. For details in the legends please see references in Fig. 17(b) in [106].

## Conclusions

In the present work, an original exploitation of the phase field approach has been proposed to simulate complex crack patterns in five types of TPMS open cells under compression. The TPMS unit cells of Schwarz Primitive, Schoen Gyroid, Schoen-I-WP, Schwarz Diamond and Neovius were mathematically generated and virtually tested in compression. By choosing an aluminium alloy as base material of the open foams, a mesh sensitivity evaluation was carried out for an increasing spatial discretization refinement via stress–strain responses. Consequently, crack sites, nucleation, propagation, branching and deformation behaviour of TPMS unit cells were computationally characterized and predicted. Moreover, from the numerical campaign, the role of the volume fraction has carefully investigated. For this purpose, detailed comparative analyses were finally proposed within the Ashby diagrams relating

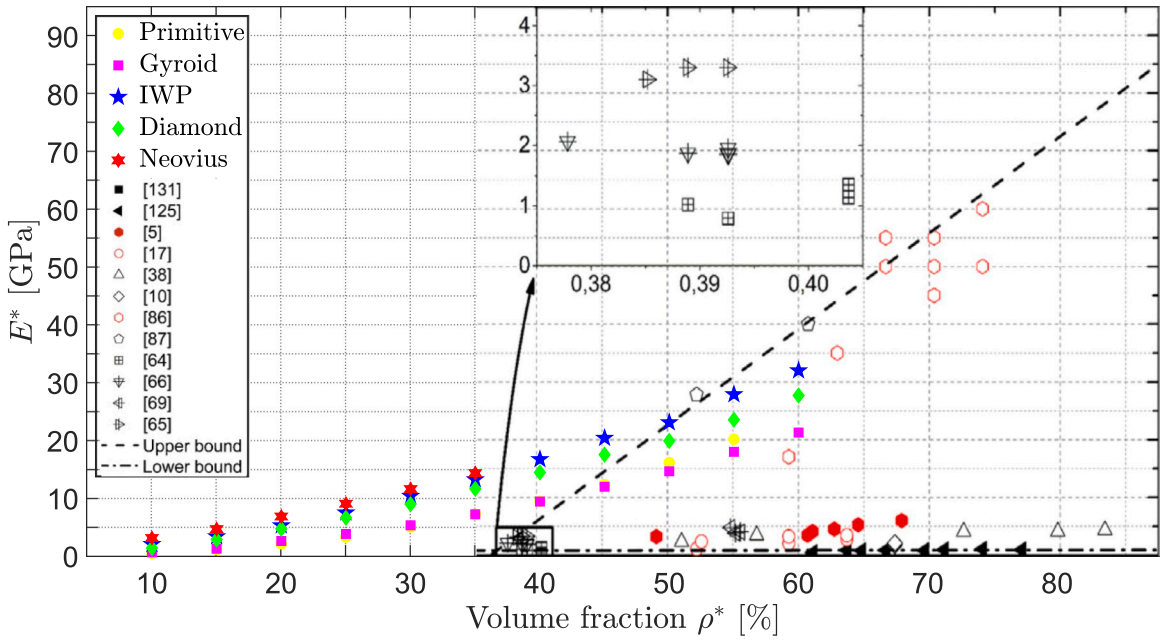


**Fig. 20.** Comparison between the predicted Young's modulus $E^*$ of TPMS foams and those of the open cell Aluminium alloy foams, vs. the volume fraction $\rho^*$. Experimental data of Aluminium foams are taken from [108]. For details in the legends please see references in Fig. 6 in [108].

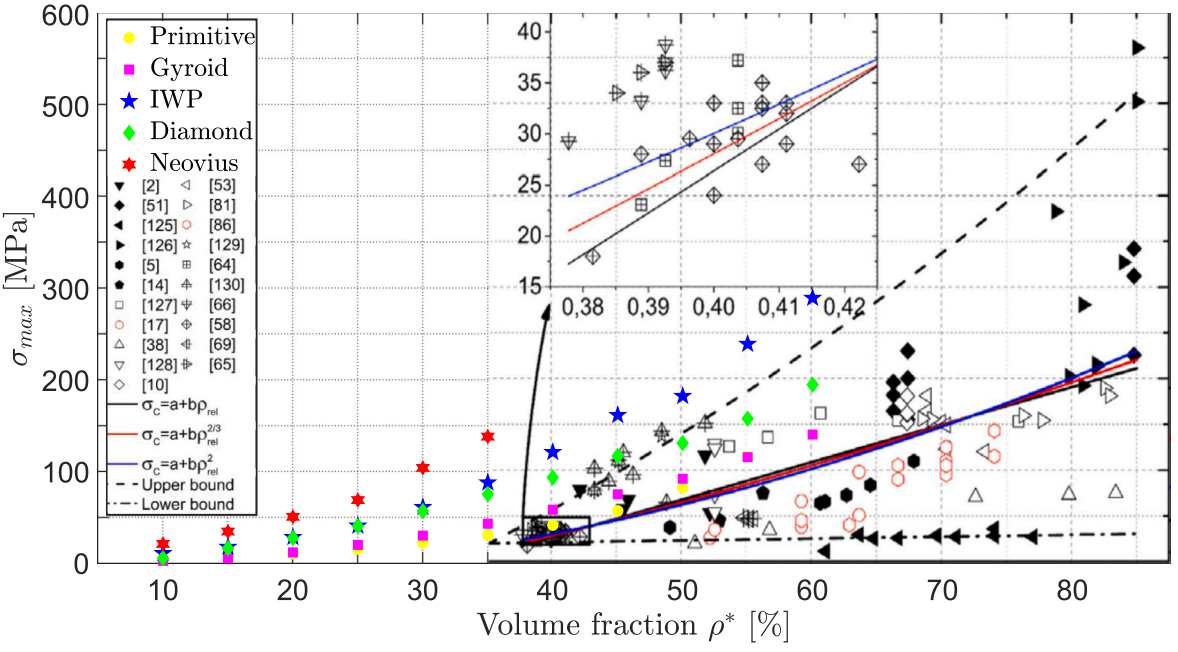


**Fig. 21.** Comparison between the predicted compressive strength $\sigma_{max,c}$ of TPMS foams and those of the open cell Aluminium alloy foams, vs. the volume fraction $\rho^*$. Experimental data of Aluminium foams are taken from [108]. For details in the legends please see references in Fig. 3 in [108].

the apparent Young's modulus in compression and the apparent maximum compressive stress to the volume fraction of the five TPMS unit cells.

Throughout, cracking phase field pattern could be assessed and contrasted with the recent literature in AM experiments. The numerical predictions showed good agreement concerning sites for crack nucleation and propagation in the Primitive and Gyroid open cells. Furthermore, it is well known that the deformation of the studied TPMS is dependent on the topology, material and unit cell size. The outcomes of this study also exhibited deformation behaviour driven by their specific topology, and demonstrated volume fraction independency, which is in good accordance with previous literature.

Through Ashby plots, a comparison with other type of cell aluminium alloy open foams with data taken from the literature was accomplished. It must be highlighted that predictions for TPMS unit cells showed the highest compressive properties as compared to standard aluminium alloys open foams.

In essence, the hereby developed model and achieved results provide together a cutting-edge tool to evaluate and estimate brittle fracture on TPMS structures, which can hasten applications of these structures in a variety of fields. For instance, it can be a useful tool on identifying weakest regions where fracture might occur in TPMS, with the aim of improving these critical sites before production by additive manufacturing. Moreover, the present phase field model can diminish the uncertainty between crack occurrence caused by defects generated from the manufacturing processes, from crack nucleation driven by the TPMS topology. In future works, the authors intend to investigate clusters of TPMS open foams, to assess emergent behaviours resulting from multiple unit cell interactions. Giving the complexity of the TPMS geometries, in order to reduce the computational time and to ensure crack estimations in the vicinity of the crack, the herein derived phase field model can also be adapted and improved by utilizing a dual-mesh adaptive refinement method. In addition, the present phase field approach can be exploited to study the effect of the base material used to manufacture these structures, through virtual testing. As such, preliminary simulations showed differences regarding crack nucleation, propagation and branching in the Gyroid unit cell structure made out of a titanium alloy from the present characterized aluminium Gyroid, which may indicate that the material used can also play an important role on TPMS reliability. Particularly, through experimental tests in recent literature, it has been observed that post-yield mechanical properties, for instance plastic deformation and plateau stress response, are dictated by the base material of the TPMS unit cells, in spite of this fact, the presented phase field model can be further derived to exploit and validate these findings.

## CRediT authorship contribution statement

**Deison Préve:** Writing – review & editing, Writing – original draft, Investigation, Data curation, Conceptualization. **Pietro Lenarda:** Writing – original draft, Visualization, Validation, Supervision, Software, Formal analysis, Data curation. **Ian Maskery:** Supervision, Methodology, Investigation, Funding acquisition. **Marco Paggi:** Supervision, Project administration, Methodology, Investigation, Funding acquisition, Formal analysis.

## Declaration of competing interest

The authors declare that they have no known competing financial interests or personal relationships that could have appeared to influence the work reported in this paper.

## Data availability

Data will be made available on request.

## Acknowledgements

DP gratefully acknowledges financial support by the Erasmus+ Programme of the European Union, no. 2020-1-IT02-KA103-078114. This work has been partially supported by the DM, Italy n. 289, 25-03-2021 –Linee generali d'indirizzo della programmazione triennale del sistema universitario per il triennio 2021–2023 (art. 3 co.3, UK)– Joint program "Le Scuole Superiori ad Ordinamento Speciale: istituzioni a servizio del Paese", CUP D67G22000130001, through the project "Scientific computing for natural sciences, social sciences, and applications: methodological and technological development".

## Appendix. Mesh sensitivity analysis

With the aim of reducing the computation time of numerical simulations, which are demanding in 3D, a mesh sensitivity analysis has been carried out throughout the analysis of the outcomes of the compressive stress–strain curves for different mesh refinements of a single unit cell of the Primitive, Gyroid, IWP, Diamond and Neovius TPMS. The outcomes from the present analysis are assessed in Sections 3 and 4. For such a purpose, the material adopted for the lattices was Aluminium alloy [44]. The Young's modulus and Poisson's ratio of this material are, respectively, $E^* = 82$ GPa and $\nu = 0.33$. The fracture toughness $\mathcal{G}_c$, and the apparent tensile strength $\sigma_{\max}$, are taken from a broad range of previous evaluations through AM [109–113]. In accordance, from Eq. (17), a length scale $l_0$ is the order of $10^{-4}$ mm. The fracture toughness $\mathcal{G}_c$ is set in the order of $10^{-4}$ J/mm$^2$.

The unit cells were generated with dimensions of 8 mm × 8 mm × 8 mm each, which means that the enclosing cubic unit cell volume is $V = L^3 = 512$ mm$^3$, and the percentage volume fraction, $\rho^*$, was 20%. Force–displacement curves were numerically

**Table A.1**
Apparent Young's modulus and ultimate compressive stresses for a volume fraction of 20% from simulations, average values and standard deviations.

| TPMS | $\bar{E}^*$ [GPa] | $\sigma_{\max,c}$ [MPa] |
|---|---|---|
| Primitive | 1.99 ± 0.04 | 10.4 ± 0.6 |
| Gyroid | 2.44 ± 0.23 | 10.8 ± 2.5 |
| IWP | 5.01 ± 0.12 | 19.8 ± 3.3 |
| Diamond | 4.54 ± 0.30 | 26.5 ± 2.3 |
| Neovius | 6.98 ± 0.45 | 52.1 ± 6.2 |

predicted to compute the stress–strain curves by dividing the force by the apparent cross-sectional area $A = L^2$ and the displacement by $L$. A maximum quasi-static compressive displacement of $10^{-3}$ mm was applied along all the simulations of the lattices. The spatial discretization values $\mu$ taken to perform the mesh analysis for the Primitive unit cells were $\mu = 15$ to $\mu = 70$, for the Gyroid unit cell meshes were $\mu = 20$ to $\mu = 75$, and for the IWP, Neovius and Diamond meshes were $\mu = 25$ to $\mu = 75$, in increments of 5.

The stress–strain curves of the series of Primitive, Gyroid, IWP, Diamond and Neovius lattices are plotted in Figs. 22(a), 23(a), 24(a), 25(a) and 26(a). During loading, it can be noted a linear elastic behaviour at low strains up to the critical stress point.

The stress–strain curves of the unit cells begin to show significant deformations right after the peak compressive stress is reached, followed by a drastic drop in the curves, losing their load-bearing capacity. This characteristic is also observed in compressive tests with clusters of TPMS additively fabricated [32,33,46], although clusters of TPMS are employed and their global collapse may different from the local failure of a single cell.

Here, the apparent Young's modulus of the different discretized TPMS was found by calculating the slope of the first linear elastic region, i.e. up to $0,2\%$ strain level. Figs. 22(b), 23(b), 24(b), 25(b) and 26(b) depict how the apparent Young's modulus varies depending on mesh refinement (corresponding to a different value of $\mu$). A synthesis of the mesh sensitivity analysis for the different TPMS is provided in Tables A.2 to A.6, with the value of $\mu$, the number of finite elements, the apparent Young's modulus $E^*$, and the apparent strength $\sigma_{max,c}$.

Although to ensure an accurate estimation of fracture patterns it is necessary to have a finite element size $h = L/\mu$ of the order of $h \ll (1/5{\sim}1/10)l_0$ [84,114]. It can be noted from the previous results that the absolute error deviations from the finest meshes is quite stable even for coarser discretizations. In particular, in order to improve computational efficiency of the herein model and to ensure an accurate estimation of the crack as it evolves, a dual-mesh adaptive approach proposed in [115] can also be implemented to avoid the analysis of too fine meshes requesting very long simulations. The finest mesh discretizations chosen ensure apparent Young's moduli and maximum compressive stresses as tabulated in Table A.1, together with their respective standard deviations based on the above series of simulations at different discretizations calculated from Tables A.2 to A.6. It is also observed that among the five TPMS unit cells studied at 20% of volume fraction, the Neovius structure gives the stiffest topology, giving an average Young's modulus of $\bar{E}^* = 6.98$ GPa, and an average maximum stress of $\sigma_{\max,c} = 52.1$ MPa, followed by IWP, Diamond, Gyroid, and Primitive, the latter being the less stiff strut among all five TPMS studied, having averages of $\bar{E}^* = 1.99$ GPa and $\sigma_{\max,c} = 10.4$ MPa. In order to map and to compare the stiffness among all the five kinds of TPMS under the developed phase field scheme, in Section 4, unit cells with different volume fractions have been generated by setting one single value of discretization for each TPMS topology. Table A.1 will also be helpful as an additional guideline when setting the proper spatial discretization $\mu$ that better optimizes the relation between finer mesh and computational time in the following volume fraction analysis in Section 4, for each of the five TPMS. It can be highlighted that crack patterns through all five TPMS were independent of the spatial discretization $\mu$ simulated, nonetheless, one also can observe that the finer the meshes became, the thinner the smeared crack region became, as expected for a phase field model.

The simulations were run in parallel with a MPI implementation of FEniCS. Throughout, for the coarsest meshes, a server with 100GB of RAM and from 4 to 6 cores has been used to run from 4 to 6 MPI simulations in parallel. Simulations run from 30 min up to 20 h. For the finest meshes, different partitions have been considered. On the medium memory partition, the average RAM utilized was 200GB and from 4 to 6 cores were used, whereas the standard memory partition utilized 125GB and from 8 to 10 cores, which CPU time varying from 20 up to roughly 72 h, for both machine partitions.

Having established the present analysis, one might notice that throughout the simulations, the phase field pattern and deformation behaviour of the five TPMS unit cells studied are essentially the same for the several spatial discretizations analysed, and therefore the phase field model proposed well captures and characterizes the crack nucleation, branching, propagation and deformation mechanism. Additionally, choosing meshes near 300,000 tetrahedral elements are capable to pursuit the further analyses on volume fraction in unit cell TPMS specimens with dimensions of $8\ \text{mm} \times 8\ \text{mm} \times 8\ \text{mm}$ made in Section 4. A similar approach was taken in [48], whereas along other investigative studies [40,105,116], TPMS unit cell meshes of around 50,000 elements were sufficient to ensure finite element mesh independent results.

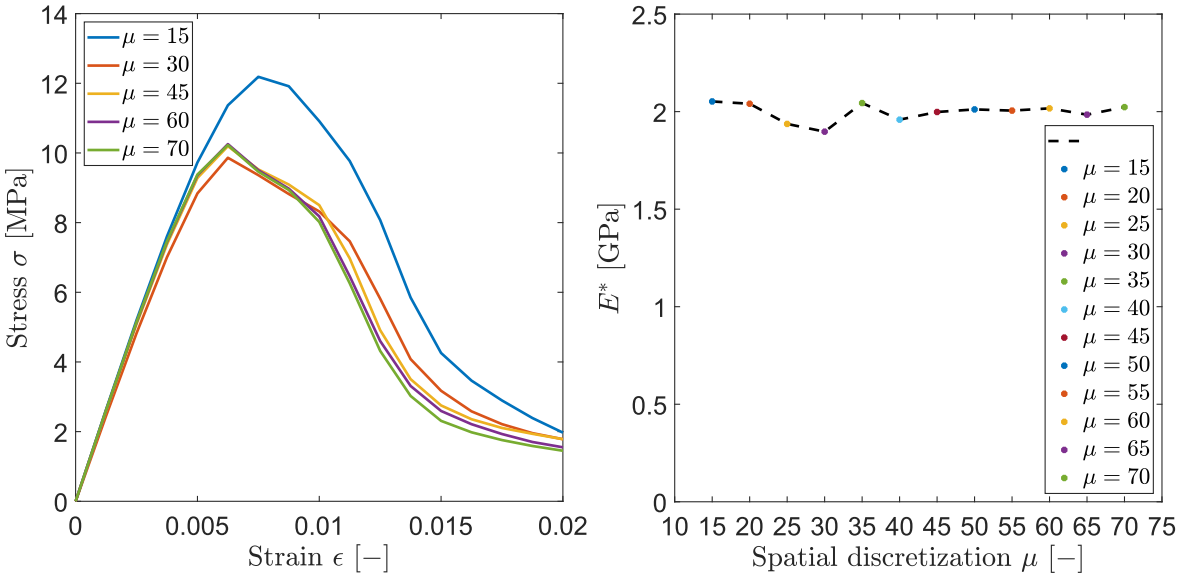


(a) Stress–strain curves for different spatial discretizations.

(b) Young's modulus dependency on the spatial discretization.

**Fig. 22.** Mesh sensitivity analysis of the Primitive unit cells at 20% volume fraction.

**Table A.2**
Primitive: Spatial discretization $\mu$; number of finite elements; apparent Young's modulus $E^*$; ultimate compressive stress $\sigma_{\max,c}$.

| $\mu$ | N. of elements | $E^*(\mu)$ [GPa] | $\sigma_{\max,c}(\mu)$ [MPa] |
|---|---|---|---|
| 15 | 21,875 | 2.05 | 12.2 |
| 20 | 48,045 | 2.04 | 10.7 |
| 25 | 68,945 | 1.93 | 10.2 |
| 30 | 1,33,611 | 1.89 | 9.9 |
| 35 | 1,94,478 | 2.04 | 10.6 |
| 40 | 2,98,375 | 1.95 | 10.0 |
| 45 | 3,94,161 | 1.99 | 10.2 |
| 50 | 4,95,644 | 2.01 | 10.3 |
| 55 | 6,21,951 | 2.00 | 10.1 |
| 60 | 7,83,464 | 2.01 | 10.3 |
| 65 | 9,04,353 | 1.98 | 10.0 |
| 70 | 11,57,245 | 2.02 | 10.2 |

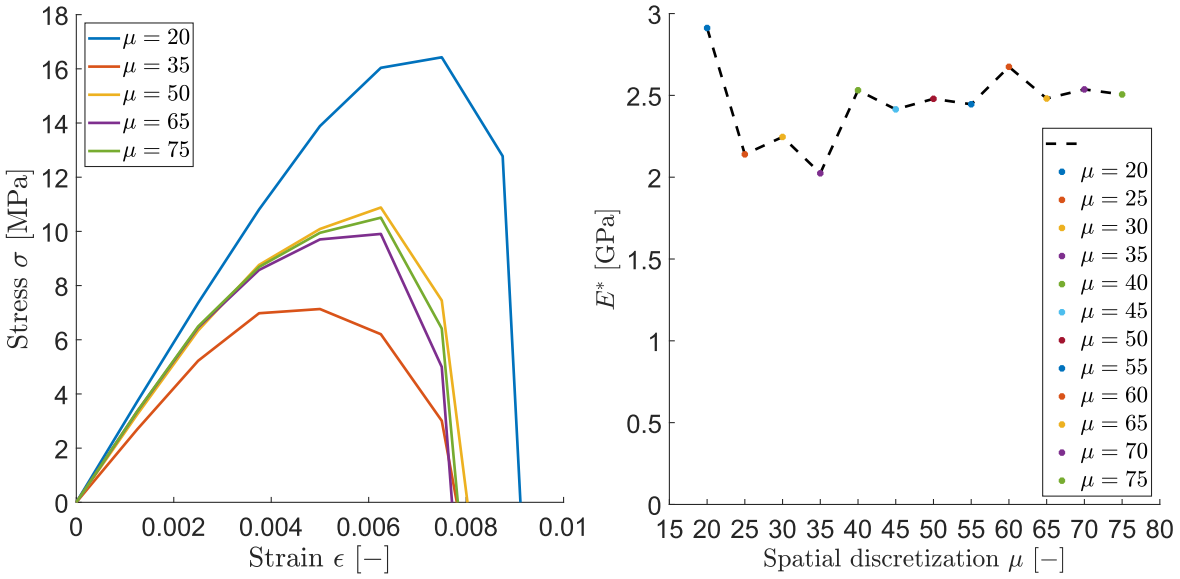


(a) Stress–strain curves for different spatial discretizations.

(b) Young's modulus dependency on the spatial discretization.

**Fig. 23.** Mesh sensitivity analysis of the Gyroid unit cells at 20% volume fraction.

**Table A.3**
Gyroid: Spatial discretization $\mu$; number of finite elements; apparent Young's modulus $E^*$; ultimate compressive stress $\sigma_{\max,c}$.

| $\mu$ | N. of elements | $E^*(\mu)$ [GPa] | $\sigma_{\max,c}(\mu)$ [MPa] |
|---|---|---|---|
| 20 | 50,425 | 2.91 | 16.43 |
| 25 | 90,900 | 2.13 | 9.73 |
| 30 | 1,46,380 | 2.24 | 10.33 |
| 35 | 2,29,317 | 2.02 | 7.13 |
| 40 | 3,06,548 | 2.53 | 10.82 |
| 45 | 4,34,392 | 2.41 | 10.21 |
| 50 | 5,50,416 | 2.47 | 10.88 |
| 55 | 7,15,508 | 2.44 | 10.68 |
| 60 | 7,88,926 | 2.67 | 12.49 |
| 65 | 10,56,405 | 2.48 | 9.91 |
| 70 | 12,57,132 | 2.53 | 10.88 |
| 75 | 15,37,369 | 2.50 | 10.51 |

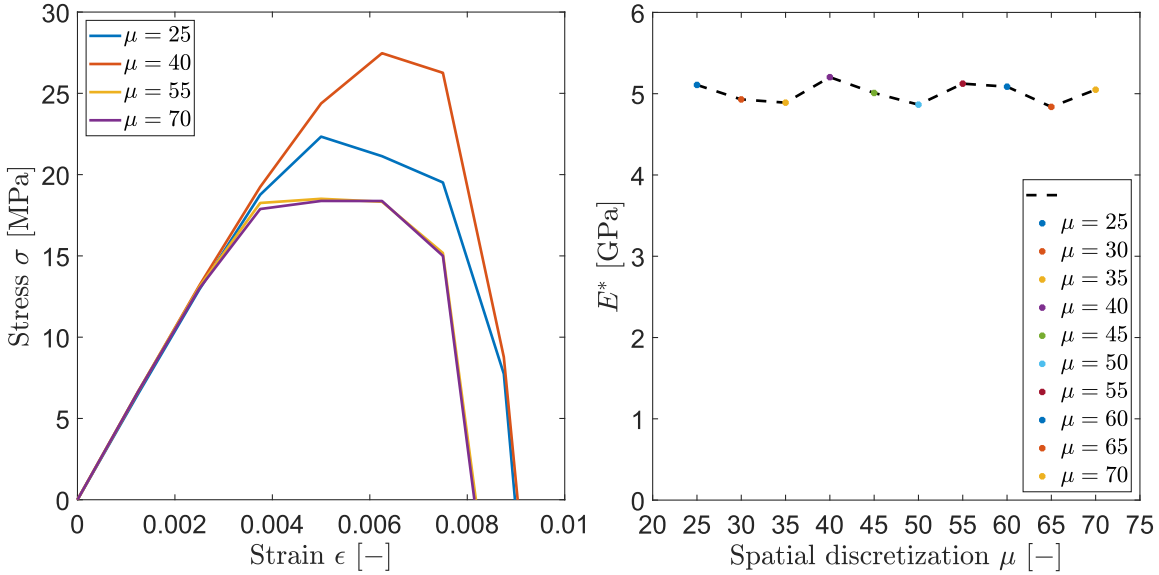


(a) Stress–strain curves of the simulated IWP unit cells at different spatial discretizations.

(b) Spatial discretization × Derived Young's modulus.

**Fig. 24.** Mesh sensitivity analysis of the IWP unit cells at 20% volume fraction.

**Table A.4**
IWP: Spatial discretization $\mu$; number of finite elements; apparent Young's modulus $E^*$; ultimate compressive stress $\sigma_{\max,c}$.

| $\mu$ | N. of elements | $E^*(\mu)$ [GPa] | $\sigma_{\max,c}(\mu)$ [MPa] |
|---|---|---|---|
| 25 | 80,317 | 5.10 | 22.3 |
| 30 | 1,41,942 | 4.92 | 17.4 |
| 35 | 2,30,306 | 4.88 | 20.9 |
| 40 | 2,94,595 | 5.20 | 27.5 |
| 45 | 4,05,429 | 5.00 | 18.3 |
| 50 | 5,58,742 | 4.86 | 16.9 |
| 55 | 6,78,209 | 5.12 | 18.5 |
| 60 | 8,71,902 | 5.08 | 21.5 |
| 65 | 10,57,063 | 4.83 | 16.5 |
| 70 | 12,30,149 | 5.04 | 18.4 |

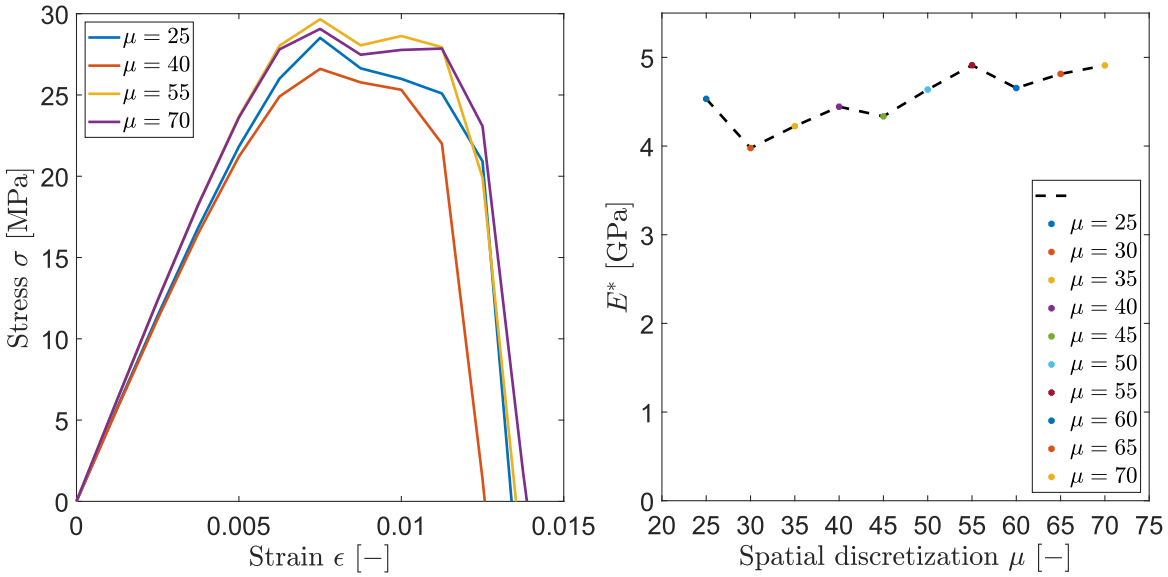


(a) Stress–strain curves for different spatial discretizations.

(b) Young's modulus dependency on the spatial discretization.

**Fig. 25.** Mesh sensitivity analysis of the Diamond unit cells at 20% volume fraction.

**Table A.5**
Diamond: Spatial discretization $\mu$; number of finite elements; apparent Young's modulus $E^*$; ultimate compressive stress $\sigma_{\max}$.

| $\mu$ | N. of elements | $E^*(\mu)$ [GPa] | $\sigma_{\max,c}(\mu)$ [MPa] |
|---|---|---|---|
| 25 | 1,01,166 | 4.53 | 28.5 |
| 30 | 1,51,999 | 3.97 | 23.0 |
| 35 | 2,27,730 | 4.22 | 25.0 |
| 40 | 3,09,889 | 4.44 | 26.6 |
| 45 | 4,73,513 | 4.33 | 23.1 |
| 50 | 5,84,342 | 4.63 | 26.7 |
| 55 | 7,16,617 | 4.91 | 29.7 |
| 60 | 9,25,827 | 4.65 | 259 |
| 65 | 10,73,706 | 4.81 | 27.1 |
| 70 | 13,86,746 | 4.90 | 29.1 |

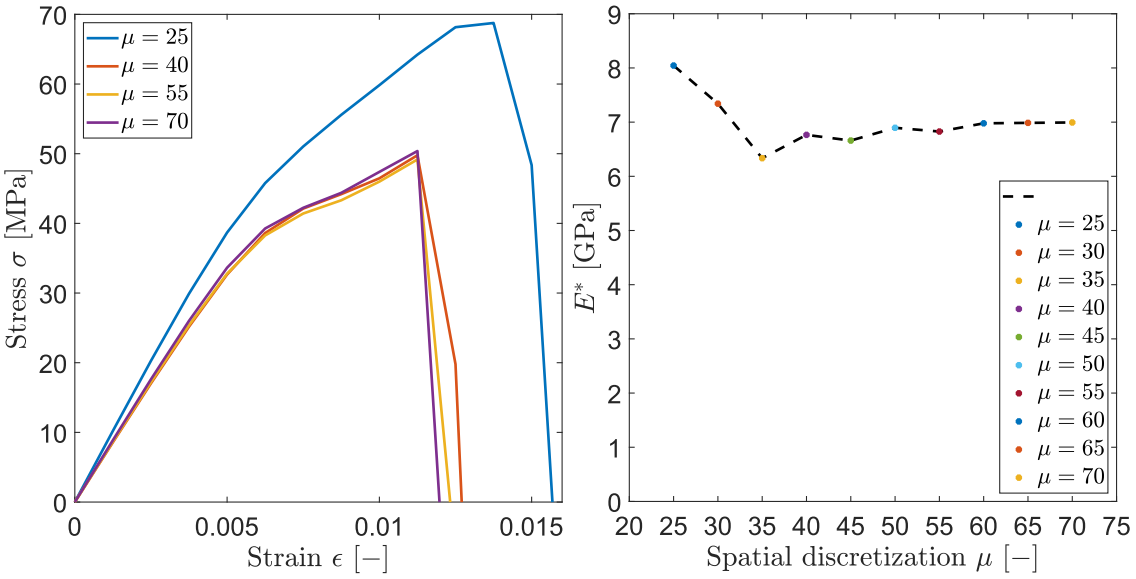


(a) Stress–strain curves for different spatial discretizations.

(b) Young's modulus dependency on the spatial discretization.

**Fig. 26.** Mesh sensitivity analysis of the Neovius unit cells at 20% volume fraction.

**Table A.6**
Neovius: Spatial discretization $\mu$; number of finite elements; apparent Young's modulus $E^*$; ultimate compressive stress $\sigma_{\max}$.

| $\mu$ | N. of elements | $E^*(\mu)$ [GPa] | $\sigma_{max,c}(\mu)$ [MPa] |
|---|---|---|---|
| 25 | 95,363 | 8,04 | 68,8 |
| 30 | 1,24,734 | 7.37 | 55.5 |
| 35 | 1,74,635 | 6.33 | 48.2 |
| 40 | 2,66,917 | 6.76 | 49.8 |
| 45 | 3,52,847 | 6.65 | 48.6 |
| 50 | 4,65,175 | 6.89 | 50.1 |
| 55 | 6,07,940 | 6.82 | 49.2 |
| 60 | 7,52,578 | 6.95 | 49.9 |
| 65 | 8,64,469 | 6.92 | 50.1 |
| 70 | 10,85,643 | 6.99 | 50.4 |

## References


[1] Do Carmo MP. Differential forms and applications. Springer Science & Business Media; 2012.
[2] Gray A, Abbena E, Salamon S. Modern differential geometry of curves and surfaces with mathematica®. Chapman and Hall/CRC; 2017.
[3] Douglas J. Solution of the problem of Plateau. Trans Amer Math Soc 1931;33(1):263–321.
[4] Winter B, Butz B, Dieker C, Schröder-Turk GE, Mecke K, Spiecker E. Coexistence of both gyroid chiralities in individual butterfly wing scales of Callophrys rubi. Proc Natl Acad Sci 2015;112(42):12911–6.
[5] Nissen H-U. Crystal orientation and plate structure in echinoid skeletal units. Science 1969;166(3909):1150–2.
[6] Hyde S, Blum Z, Landh T, Lidin S, Ninham BW, Andersson S, et al. The language of shape: The role of curvature in condensed matter: Physics, chemistry and biology. Elsevier; 1996.
[7] Galusha JW, Richey LR, Jorgensen MR, Gardner JS, Bartl MH. Study of natural photonic crystals in beetle scales and their conversion into inorganic structures via a sol–gel bio-templating route. J Mater Chem 2010;20(7):1277–84.
[8] Schröder-Turk GE, Wickham S, Averdunk Holger, Brink F, Gerald JD Fitz, Poladian L, et al. The chiral structure of porous chitin within the wing-scales of Callophrys rubi. J Struct Biol 2011;174(2):290–5.
[9] Kapfer SC, Hyde ST, Mecke K, Arns CH, Schröder-Turk GE. Minimal surface Scaffold designs for tissue engineering. Biomaterials 2011;32(29):6875–82.
[10] Jinnai H, Nishikawa Y, Ito M, Smith SD, Agard DA, Spontak RJ. Topological similarity of sponge-like bicontinuous morphologies differing in length scale. Adv Mater 2002;14(22):1615–8.
[11] Jinnai H, Watashiba H, Kajihara T, Nishikawa Y, Takahashi M, Ito M. Surface curvatures of trabecular bone microarchitecture. Bone 2002;30(1):191–4.
[12] Olmsted PD, Milner ST. Strong segregation theory of bicontinuous phases in block copolymers. Macromolecules 1998;31(12):4011–22.
[13] Wohlgemuth M, Yufa N, Hoffman J, Thomas EL. Triply periodic bicontinuous cubic microdomain morphologies by symmetries. Macromolecules 2001;34(17):6083–9.
[14] Torquato S, Donev A. Minimal surfaces and multifunctionality. Proc R Soc Lond Ser A Math Phys Eng Sci 2004;460(2047):1849–56.
[15] Asbai-Ghoudan R, de Galarreta SR, Rodriguez-Florez N. Analytical model for the prediction of permeability of triply periodic minimal surfaces. J Mech Behav Biomed Mater 2021;104804.

[16] Qureshi ZA, Elnajjar E, Al-Ketan O, Al-Rub RA, Al-Omari SB. Heat transfer performance of a finned metal foam-phase change material (FMF-PCM) system incorporating triply periodic minimal surfaces (TPMS). Int J Heat Mass Transfer 2021;170:121001.
[17] Qureshi ZA, Al-Omari SAB, Elnajjar E, Al-Ketan O, Al-Rub RA. Using triply periodic minimal surfaces (TPMS)-based metal foams structures as skeleton for metal-foam-PCM composites for thermal energy storage and energy management applications. Int Commun Heat Mass Transfer 2021;124:105265.
[18] Iyer J, Moore T, Nguyen D, Roy P, Stolaroff J. Heat transfer and pressure drop characteristics of heat exchangers based on triply periodic minimal and periodic nodal surfaces. Appl Therm Eng 2022;118192.
[19] Maskery I, Sturm L, Aremu AO, Panesar A, Williams CB, Tuck CJ, et al. Insights into the mechanical properties of several triply periodic minimal surface lattice structures made by polymer additive manufacturing. Polymer 2018;152:62–71.
[20] Sychov MM, Lebedev LA, Dyachenko SV, Nefedova LA. Mechanical properties of energy-absorbing structures with triply periodic minimal surface topology. Acta Astronaut 2018;150:81–4.
[21] Yoo D. New paradigms in internal architecture design and freeform fabrication of tissue engineering porous Scaffolds. Med Eng Phys 2012;34(6):762–76.
[22] Afshar M, Anaraki A Pourkamali, Montazerian H, Kadkhodapour J. Additive manufacturing and mechanical characterization of graded porosity Scaffolds designed based on triply periodic minimal surface architectures. J Mech Behav Biomed Mater 2016;62:481–94.
[23] Ataee A, Li Y, Brandt M, Wen C. Ultrahigh-strength titanium gyroid Scaffolds manufactured by selective laser melting (SLM) for bone implant applications. Acta Mater 2018;158:354–68.
[24] Karimipour-Fard P, Behravesh AH, Jones-Taggart H, Pop-Iliev R, Rizvi G. Effects of design, porosity and biodegradation on mechanical and morphological properties of additive-manufactured triply periodic minimal surface Scaffolds. J Mech Behav Biomed Mater 2020;112:104064.
[25] Kadkhodapour J, Montazerian H, Darabi A Ch, Zargarian A, Schmauder S. The relationships between deformation mechanisms and mechanical properties of additively manufactured porous biomaterials. J Mech Behav Biomed Mater 2017;70:28–42.
[26] Yánez A, Cuadrado A, Martel O, Afonso H, Monopoli D. Gyroid porous titanium structures: A versatile solution to be used as Scaffolds in bone defect reconstruction. Mater Des 2018;140:21–9.
[27] Yang L, Yan C, Han C, Chen P, Yang S, Shi Y. Mechanical response of a triply periodic minimal surface cellular structures manufactured by selective laser melting. Int J Mech Sci 2018;148:149–57.
[28] Bobbert FSL, Lietaert K, Eftekhari AA, Pouran B, Ahmadi SM, Weinans H, et al. Additively manufactured metallic porous biomaterials based on minimal surfaces: A unique combination of topological, mechanical, and mass transport properties. Acta Biomater 2017;53:572–84.
[29] Castro APG, Pires T, Santos JE, Gouveia BP, Fernandes PR. Permeability versus design in TPMS Scaffolds. Materials 2019;12(8):1313.
[30] Santos J, Pires T, Gouveia BP, Castro APG, Fernandes PR. On the permeability of TPMS Scaffolds. J Mech Behav Biomed Mater 2020;110:103932.
[31] Pires T, Santos J, Ruben RB, Gouveia BP, Castro APG, Fernandes PR. Numerical-experimental analysis of the permeability-porosity relationship in triply periodic minimal surfaces Scaffolds. J Biomech 2021;117:110263.
[32] Abueidda DW, Bakir M, Al-Rub RKA, Bergström JS, Sobh NA, Jasiuk I. Mechanical properties of 3D printed polymeric cellular materials with triply periodic minimal surface architectures. Mater Des 2017;122:255–67.
[33] Al-Ketan O, Rowshan R, Al-Rub RKA. Topology-mechanical property relationship of 3D printed strut, skeletal, and sheet based periodic metallic cellular materials. Addit Manuf 2018;19:167–83.
[34] Keshavarzan M, Kadkhodaei M, Badrossamay M, Ravari MRK. Investigation on the failure mechanism of triply periodic minimal surface cellular structures fabricated by vat photopolymerization additive manufacturing under compressive loadings. Mech Mater 2020;140:103150.
[35] Novak N, Al-Ketan O, Krstulović-Opara L, Rowshan R, Al-Rub RKA, Vesenjak M, et al. Quasi-static and dynamic compressive behaviour of sheet TPMS cellular structures. Compos Struct 2021;266:113801.
[36] Al-Ketan O, Rezgui R, Rowshan R, Du H, Fang NX, Abu Al-Rub RK. Microarchitected stretching-dominated mechanical metamaterials with minimal surface topologies. Adv Energy Mater 2018;20(9):1800029.
[37] Bonatti C, Mohr D. Smooth-shell metamaterials of cubic symmetry: Anisotropic elasticity, yield strength and specific energy absorption. Acta Mater 2019;164:301–21.
[38] Torres-Sanchez C, Borgman JM, Sargeant B, Bell H, Alabort E, Lindsay C, et al. Comparison of selective laser melted commercially pure titanium sheet-based triply periodic minimal surfaces and trabecular-like strut-based Scaffolds for tissue engineering. Adv Energy Mater 2021;2100527.
[39] Cai J, Ma Y, Deng Z. On the effective elastic modulus of the ribbed structure based on Schwarz primitive triply periodic minimal surface. Thin-Walled Struct 2022;170:108642.
[40] Montazerian H, Davoodi E, Asadi-Eydivand M, Kadkhodapour J, Solati-Hashjin M. Porous Scaffold internal architecture design based on minimal surfaces: a compromise between permeability and elastic properties. Mater Des 2017;126:98–114.
[41] Yu S, Sun J, Bai J. Investigation of functionally graded TPMS structures fabricated by additive manufacturing. Mater Des 2019;182:108021.
[42] Yan C, Hao L, Hussein A, Young P. Ti–6Al–4V triply periodic minimal surface structures for bone implants fabricated via selective laser melting. J Mech Behav Biomed Mater 2015;51:61–73.
[43] Yan C, Hao L, Hussein A, Young P, Huang J, Zhu W. Microstructure and mechanical properties of aluminium alloy cellular lattice structures manufactured by direct metal laser sintering. Mater Sci Eng A 2015;628:238–46.
[44] Maskery I, Aboulkhair NT, Aremu AO, Tuck CJ, Ashcroft IA. Compressive failure modes and energy absorption in additively manufactured double gyroid lattices. Addit Manuf 2017;16:24–9.
[45] Al-Ketan O, Lee D-W, Rowshan R, Al-Rub RKA. Functionally graded and multi-morphology sheet TPMS lattices: Design, manufacturing, and mechanical properties. J Mech Behav Biomed Mater 2020;102:103520.
[46] Sun Q, Sun J, Guo K, Wang L. Compressive mechanical properties and energy absorption characteristics of SLM fabricated Ti6Al4V triply periodic minimal surface cellular structures. Mech Mater 2022;104241.
[47] Speirs M, Van Hooreweder B, Van Humbeeck J, Kruth J-P. Fatigue behaviour of NiTi shape memory alloy Scaffolds produced by SLM, a unit cell design comparison. J Mech Behav Biomed Mater 2017;70:53–9.
[48] Kadkhodapour J, Montazerian H, Darabi A Ch, Anaraki AP, Ahmadi SM, Zadpoor AA, et al. Failure mechanisms of additively manufactured porous biomaterials: Effects of porosity and type of unit cell. J Mech Behav Biomed Mater 2015;50:180–91.
[49] AlMahri S, Santiago R, Lee D-W, Ramos H, Alabdouli H, Alteneiji M, et al. Evaluation of the dynamic response of triply periodic minimal surfaces subjected to high strain-rate compression. Addit Manuf 2021;46:102220.
[50] Francfort GA, Marigo J-J. Revisiting brittle fracture as an energy minimization problem. J Mech Phys Solids 1998;46(8):1319–42.
[51] Ambrosio L, Tortorelli VM. Approximation of functional depending on jumps by elliptic functional via T-convergence. Comm Pure Appl Math 1990;43(8):999–1036.
[52] Bourdin B, Francfort GA, Marigo J-J. Numerical experiments in revisited brittle fracture. J Mech Phys Solids 2000;48(4):797–826.
[53] Reinoso J, Paggi M, Linder C. Phase field modeling of brittle fracture for enhanced assumed strain shells at large deformations: Formulation and finite element implementation. Comput Mech 2017;59(6):981–1001.
[54] Dean A, Kumar PK Asur Vijaya, Reinoso J, Gerendt C, Paggi M, Mahdi E, et al. A multi phase-field fracture model for long fiber reinforced composites based on the puck theory of failure. Compos Struct 2020;251:112446.
[55] Kumar PK Asur Vijaya, Dean A, Reinoso J, Lenarda P, Paggi M. Phase field modeling of fracture in Functionally Graded Materials: $\Gamma$-convergence and mechanical insight on the effect of grading. Thin-Walled Struct 2021;159:107234.
[56] Amiri F, Millán D, Shen Y, Rabczuk T, Arroyo M. Phase-field modeling of fracture in linear thin shells. Theor Appl Fract Mech 2014;69:102–9.

[57] Lee D-W, Khan KA, Al-Rub RKA. Stiffness and yield strength of architectured foams based on the Schwarz primitive triply periodic minimal surface. Int J Plast 2017;95:1–20.
[58] Castro APG, Santos J, Pires T, Fernandes PR. Micromechanical behavior of TPMS Scaffolds for bone tissue engineering. Macromol Mater Eng 2020;305(12):2000487.
[59] Feng J, Liu B, Lin Z, Fu J. Isotropic porous structure design methods based on triply periodic minimal surfaces. Mater Des 2021;210:110050.
[60] Braides A, et al. Approximation of free-discontinuity problems, no. 1694. Springer Science & Business Media; 1998.
[61] Miehe C, Hofacker M, Welschinger F. A phase field model for rate-independent crack propagation: Robust algorithmic implementation based on operator splits. Comput Methods Appl Mech Engrg 2010;199(45–48):2765–78.
[62] Alnæs MS, Hake J, Kirby RC, Langtangen HP, Logg A, Wells GN. The fenics manual. 2011, FEniCS Project, Version October 31st, 36.
[63] Ashby MF, Gibson LJ. Cellular solids: structure and properties. Cambridge, UK: Press Syndicate of the University of Cambridge; 1997, p. 175–231.
[64] Ashby MF. The properties of foams and lattices. Phil Trans R Soc A 2006;364(1838):15–30.
[65] Bonnet O. Note sur la théorie générale des surfaces. CR Acad Sci Paris 1853;37:529–32.
[66] Karcher H. The triply periodic minimal surfaces of Alan Schoen and their constant mean curvature companions. Manuscripta Math 1989;64(3):291–357.
[67] Pinkall U, Polthier K. Computing discrete minimal surfaces and their conjugates. Experiment Math 1993;2(1):15–36.
[68] Karcher H, Polthier K. Construction of triply periodic minimal surfaces. Phil Trans R Soc A 1996;354(1715):2077–104.
[69] Gandy PJF, Cvijović D, Mackay AL, Klinowski J. Exact computation of the triply periodic D (diamond') minimal surface. Chem Phys Lett 1999;314(5–6):543–51.
[70] Gandy PJF, Klinowski J. Exact computation of the triply periodic G (Gyroid') minimal surface. Chem Phys Lett 2000;321(5–6):363–71.
[71] Gandy PJF, Klinowski J. Exact computation of the triply periodic Schwarz P minimal surface. Chem Phys Lett 2000;322(6):579–86.
[72] Von Schnering HG, Nesper R. Nodal surfaces of Fourier series: fundamental invariants of structured matter. Z Phys B 1991;83(3):407–12.
[73] Mackay AL. Periodic minimal surfaces from finite element methods. Chem Phys Lett 1994;221(3–4):317–21.
[74] Lambert CA, Radzilowski LH, Thomas EL. Triply periodic level surfaces as models for cubic tricontinuous block copolymer morphologies. Phil Trans R Soc A 1996;354(1715):2009–23.
[75] Gandy PJF, Bardhan S, Mackay AL, Klinowski J. Nodal surface approximations to the P, G, D and I-WP triply periodic minimal surfaces. Chem Phys Lett 2001;336(3–4):187–95.
[76] GóźdŹ Wojciech T, Hołyst R. Triply periodic surfaces and multiply continuous structures from the Landau model of microemulsions. Phys Rev E 1996;54(5):5012.
[77] Jung Y, Torquato S. Fluid permeabilities of triply periodic minimal surfaces. Phys Rev E 2005;72(5):056319.
[78] Torquato S, Hyun S, Donev A. Multifunctional composites: Optimizing microstructures for simultaneous transport of heat and electricity. Phys Rev Lett 2002;89(26):266601.
[79] Chen Z, Xie YM, Wu X, Wang Z, Li Q, Zhou S. On hybrid cellular materials based on triply periodic minimal surfaces with extreme mechanical properties. Mater Des 2019;183:108109.
[80] Abueidda DW, Al-Rub RKA, Dalaq AS, Lee D-W, Khan KA, Jasiuk I. Effective conductivities and elastic moduli of novel foams with triply periodic minimal surfaces. Mech Mater 2016;95:102–15.
[81] Melchels FPW, Bertoldi K, Gabbrielli R, Velders AH, Feijen J, Grijpma DW. Mathematically defined tissue engineering Scaffold architectures prepared by stereolithography. Biomaterials 2010;31(27):6909–16.
[82] Ma S, Song K, Lan J, Ma L. Biological and mechanical property analysis for designed heterogeneous porous Scaffolds based on the refined TPMS. J Mech Behav Biomed Mater 2020;107:103727.
[83] Griffith AA. VI. The phenomena of rupture and flow in solids. Philos Trans R Soc Lond Ser A 1921;221(582–593):163–98.
[84] Bourdin B, Francfort GA, Marigo J-J. The variational approach to fracture. J Elasticity 2008;91(1):5–148.
[85] Amor H, Marigo J-J, Maurini C. Regularized formulation of the variational brittle fracture with unilateral contact: Numerical experiments. J Mech Phys Solids 2009;57(8):1209–29.
[86] Borden MJ, Verhoosel CV, Scott MA, Hughes TJR, Landis CM. A phase-field description of dynamic brittle fracture. Comput Methods Appl Mech Engrg 2012;217:77–95.
[87] Dal Maso G. An introduction to $\Gamma$-convergence, vol. 8. Springer Science & Business Media; 2012.
[88] Braides A. $\Gamma$-convergence for beginners. Oxford lecture series in mathematics and its applications, vol. 22, 2002.
[89] Cavuoto R, Lenarda P, Misseroni D, Paggi M, Bigoni D. Failure through crack propagation in components with holes and notches: An experimental assessment of the phase field model. Int J Solids Struct 2022;111798.
[90] Pham K, Amor H, Marigo J-J, Maurini C. Gradient damage models and their use to approximate brittle fracture. Int J Damage Mech 2011;20(4):618–52.
[91] Pham K, Marigo J-J, Maurini C. The issues of the uniqueness and the stability of the homogeneous response in uniaxial tests with gradient damage models. J Mech Phys Solids 2011;59(6):1163–90.
[92] Martínez-Pañeda E, Golahmar A, Niordson CF. A phase field formulation for hydrogen assisted cracking. Comput Methods Appl Mech Engrg 2018;342:742–61.
[93] Zhang X, Vignes C, Sloan SW, Sheng D. Numerical evaluation of the phase-field model for brittle fracture with emphasis on the length scale. Comput Mech 2017;59(5):737–52.
[94] Tanné E, Li T, Bourdin B, Marigo J-J, Maurini C. Crack nucleation in variational phase-field models of brittle fracture. J Mech Phys Solids 2018;110:80–99.
[95] Maskery I, Parry LA, Padrão D, Hague RJM, Ashcroft IA. Flatt Pack: A research-focussed lattice design program. Addit Manuf 2022;49:102510.
[96] Nguyen BD, Han SCl, Jung YC, Kang K. Design of the P-surfaced shellular, an ultra-low density material with micro-architecture. Comput Mater Sci 2017;139:162–78.
[97] Han SC, Choi JM, Liu G, Kang K. A microscopic shell structure with Schwarz's D-surface. Sci Rep 2017;7(1):1–8.
[98] Pongiman R. Hypermesh introduction pre-processing for finite element analysis. Altair University; 2014.
[99] Geuzaine C, Remacle J-F. GMSH: A 3-D finite element mesh generator with built-in pre-and post-processing facilities. Internat J Numer Methods Engrg 2009;79(11):1309–31.
[100] Mandal TK, Nguyen VP, Wu J-Y. Length scale and mesh bias sensitivity of phase-field models for brittle and cohesive fracture. Eng Fract Mech 2019;217:106532.
[101] Dhondt G. Effect of contact between the crack faces on crack propagation. In: Key engineering materials, vol. 577. Trans Tech Publ; 2014, p. 61–4.
[102] Maas SA, Ellis BJ, Rawlins DS, Weiss JA. Finite element simulation of articular contact mechanics with quadratic tetrahedral elements. J Biomech 2016;49(5):659–67.
[103] Zhu JZ, Zienkiewicz OC. A posteriori error estimation and three-dimensional automatic mesh generation. Finite Elem Anal Des 1997;25(1–2):167–84.
[104] Bremberg D, Dhondt G. Automatic crack-insertion for arbitrary crack growth. Eng Fract Mech 2008;75(3–4):404–16.
[105] Krishnan K, Lee D-W, Al Teneji M, Al-Rub RKA. Effective stiffness, strength, buckling and anisotropy of foams based on nine unique triple periodic minimal surfaces. Int J Solids Struct 2022;111418.
[106] Al-Ketan O, Abu A-R Rashid K. Multifunctional mechanical metamaterials based on triply periodic minimal surface lattices. Adv Energy Mater 2019;21(10):1900524.

[107] Al-Ketan O, Al-Rub RKA, Rowshan R. The effect of architecture on the mechanical properties of cellular structures based on the IWP minimal surface. J Mater Res 2018;33(3):343–59.
[108] Orbulov IN, Szlancsik A. On the mechanical properties of aluminum matrix syntactic foams. Adv Energy Mater 2018;20(5):1700980.
[109] Hitzler L, Hirsch J, Schanz J, Heine B, Merkel M, Hall W, et al. Fracture toughness of selective laser melted AlSi10Mg. Proc Inst Mech Eng L 2019;233(4):615–21.
[110] Tu X, Ray A, Ghosh S. A coupled crystal plasticity FEM and phase-field model for crack evolution in microstructures of 7000 series aluminum alloys. Eng Fract Mech 2020;230:106970.
[111] Liu Q, Wu H, Paul MJ, He P, Peng Z, Gludovatz B, et al. Machine-learning assisted laser powder bed fusion process optimization for AlSi10Mg: New microstructure description indices and fracture mechanisms. Acta Mater 2020;201:316–28.
[112] Paul MJ, Liu Q, Best JP, Li X, Kruzic JJ, Ramamurty U, et al. Fracture resistance of AlSi10Mg fabricated by laser powder bed fusion. Acta Mater 2021;211:116869.
[113] Wu Z, Wu S, Bao J, Qian W, Karabal S, Sun W, et al. The effect of defect population on the anisotropic fatigue resistance of AlSi10Mg alloy fabricated by laser powder bed fusion. Int J Fatigue 2021;151:106317.
[114] Wu J-Y. A unified phase-field theory for the mechanics of damage and quasi-brittle failure. J Mech Phys Solids 2017;103:72–99.
[115] Goswami S, Anitescu C, Rabczuk T. Adaptive phase field analysis with dual hierarchical meshes for brittle fracture. Eng Fract Mech 2019;218:106608.
[116] Maskery I, Aremu AO, Parry L, Wildman RD, Tuck CJ, Ashcroft IA. Effective design and simulation of surface-based lattice structures featuring volume fraction and cell type grading. Mater Des 2018;155:220–32.